Brief and localized pulsed transcranial photobiomodulation cumulatively increases EEG power across the brain in healthy young adults

Alicia A. Mathew[1,2], Hannah Van Lankveld[1,3], Xiaole Z. Zhong[1,3], Joanna X. Chen[1,3], Sophie Niculescu[1], Reza Zomorrodi[4,5], and J. Jean Chen[1,2,3]

[1]*Rotman Research Institute, Baycrest Health Sciences, Toronto, ON, Canada;*
[2]*Department of Medical Biophysics, University of Toronto, Toronto, ON, Canada;*
[3]*Department of Biomedical Engineering, University of Toronto, Toronto, ON, Canada;*
[4]*Vielight Inc., Toronto, ON, Canada;*
[5]*Temerty Centre for Therapeutic Brain Intervention, Center for Addiction and Mental Health, Toronto, ON, Canada*

ABSTRACT

Introduction: Transcranial photobiomodulation (tPBM) relies on the photochemical stimulation of mitochondrial processes and has already demonstrated some ability to improve human cognition. However, it remains unclear how tPBM modulates neural oscillatory activity in real-time and how stimulation parameters and individual characteristics affect these responses. Capturing these dynamics is essential to understanding how tPBM's photochemical effects translate into effective neuromodulation, especially in diverse populations.
Methods: Our study provides the first evidence of a cumulative increase in the power of neuro-electric oscillations in healthy humans in 46 healthy young adults with diverse skin tones underwent 4 minutes of pulsed tPBM using varying laser parameters, including two wavelengths (808/1064 nm), two pulsation frequencies (10/40 Hz), and three irradiances (100/150/200 mW/cm^2). To capture "online" and "offline" effects, we analyzed minute-by-minute baseline-normalized frequency band power and used mixed-effects modeling to uncover significant predictors of these responses among laser parameters, skin tone, and sex.
Results: tPBM elicited frequency-band specific modulations in EEG power beginning near the stimulation site and propagating posteriorly over several minutes. Increases were cumulative with time, consistent with past fNIRS findings. They were also strongest and most sustained in beta/gamma bands, consistent with past findings of cognitive improvement. Significant parameter effects included stronger high-frequency responses at 808 nm and at 150 mW/cm^2, wavelength-dependent frequency effects, larger responses in lighter skin, and parameter-specific sex differences.
Conclusion: Both laser parameters and biological factors interact to shape tPBM's spatial and temporal neuromodulation profile and hence, parameter selection is crucial for achieving specific outcomes. Our findings uncover the manner in which tPBM induces neuronal changes, and contribute to a framework for creating more informed and personalized tPBM protocols.

1 INTRODUCTION

The brain can be non-invasively modulated in many ways to improve health and cognition – through electrical, magnetic, acoustic, and more recently, light stimulation. Among these, transcranial photobiomodulation (tPBM) is a promising treatment that harnesses light to enhance brain metabolism and function, with various studies already demonstrating improved cognitive performance across attention, reaction time, memory, and executive function in younger and older adults after single and repeated tPBM sessions (Chan et al., 2019; Gonzalez-Lima & Barrett, 2014; Vargas et al., 2017).

tPBM delivers photons in the red to near-infrared (NIR) range (600-1100 nm) through the scalp to interact with light-absorbing mitochondrial structures called chromophores, typically cytochrome c oxidase (CCO). This leads to cascades of photochemical and photophysical processes in and around neurons that boost oxidative phosphorylation, adenosine triphosphate (ATP) synthesis, and nitric oxide (NO) dissociation alongside downstream safeguards against neuroinflammation and oxidative stress (de Freitas & Hamblin, 2016; Wong-Riley et al., 2005) which ultimately promote brain health. Within this physiological framework, the brain's real-time neural oscillatory response to tPBM is increasingly being explored to uncover how tPBM's photochemical effects translate to beneficial neuromodulation.

Electroencephalography (EEG) offers a direct measure of cortical electrical activity and can track changes in brain oscillations across canonical frequency bands: delta, theta, alpha, beta, and gamma (Berger, 1929; Nunez & Srinivasan, 2005; Thut, Miniussi, & Gross, 2012). Each band reflects distinct functional states of the brain: slower rhythms such as delta/theta dominate during sleep and restorative processes (Herweg et al., 2016; Karakaş, 2020; Klimesch, 1999; Klimesch et al., 2001; Léger et al., 2018; Reddy & van der Werf, 2020), while faster beta/gamma oscillations are closely linked to higher cognition (Engel & Fries, 2010; Gola et al., 2012; Miller et al., 2018; Palacios-García et al., 2021; Schmidt et al., 2019). By analyzing EEG frequency band power, the oscillatory strength within each frequency range, we can infer how tPBM modulates low- and high-frequency dynamics over time.

Recent EEG-tPBM work in healthy humans shows tPBM's effects across various protocols and parameters. Targeting the default mode network (DMN) with 810-nm light pulsed at 40 Hz, Zomorrodi et al. observed frequency-specific modulation: reduced delta/theta power and higher alpha to gamma power (Zomorrodi et al., 2019). Similarly, studies using continuous 1064-nm tPBM to the right prefrontal cortex (rPFC) have consistently reported progressive increases in alpha/beta power that partially persist into the post-stimulation period (Pruitt et al., 2024; Shahdadian et al., 2022; X. Wang et al., 2019; X. Wang et al., 2021). Overall, across protocols, the largest effects have typically emerged in the alpha to gamma bands, with power changes often originating near the stimulation site and spreading posteriorly over time (Pruitt et al., 2024; Shahdadian et al., 2022; X. Wang et al., 2019).

Despite this foundation, it remains unclear how spectral power evolves during and after stimulation, the so-called "online" and "offline" effects, which is crucial for designing more informed and targeted personalized treatment protocols. Moreover, the way tPBM's real-time neural effects are shaped by biological factors, like forehead skin tone and sex, is understudied and presents a roadblock to achieving optimal treatment outcomes in diverse populations. Our recent simulation work (Van Lankveld et al., 2025) found that melanin's strong NIR absorption could limit dose delivery in darker skin (Sandell and Zhu, 2011), yet how this modulates tPBM's neural effects is unknown. Sex dependencies in tPBM responses are also unclear and understanding these combined effects is further complicated by their interactions with core tPBM parameters: wavelength, pulsation frequency, and irradiance. Simulations reveal that 808 nm delivers more energy to the cortex through lighter skin (Cassano et al., 2019; Li et al., 2017; Van Lankveld et al., 2025), pulsation frequency may engage endogenous rhythms differently, with 10 Hz aligning with alpha oscillations and 40 Hz targeting gamma (Iaccarino et al., 2016; Zomorrodi et al., 2019), and effective irradiances of 75-250 mW/cm^2 follow biphasic mitochondrial dose-responses (Henderson and Morries, 2015; Huang et al., 2011; Y. Wang et al., 2016; Zein et al., 2018).

To study the influence of stimulation parameters and individual characteristics on the temporal and spatial pattern of tPBM-induced EEG responses, our work presents the first real-time analysis of EEG frequency band power during and post-stimulation using two wavelengths (808/1064 nm), two pulsation frequencies (10/40 Hz), and three irradiances (100/150/200 mW/cm^2).

2 METHODS

2.1 Participants and skin tone measurements

Forty-six healthy young adults (20-32 years; 24M/22F) were recruited from the Baycrest Participants Database. Exclusion criteria included neurological or physiological disorders and substance use. Ethics approval was obtained from the Baycrest Research Ethics Board and all participants gave written informed consent. To account for skin tone, forehead skin pigmentation was quantified via spectrophotometry (CM-600D, Konica Minolta, Tokyo, Japan) yielding CIE L^* b^* values to compute individual topology angles (ITA) with **Eq. 1**:

$$ITA = arctan(\frac{L^*-50}{b^*}) \times \frac{180}{\pi}. \quad (1)$$

Six readings were taken from an 8-mm area on the right forehead and averaged per participant. Higher ITAs indicate lighter skin, specifically lower levels of eumelanin, the main chromophore contributing to skin tone. ITA was treated continuously in analyses but stratified into three groups to ensure balance during recruitment (**Figure 1**).

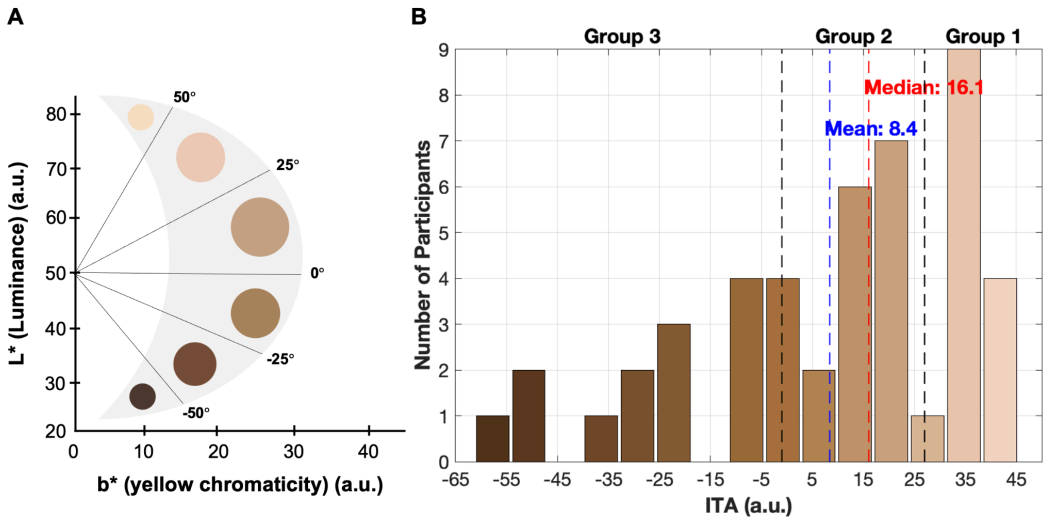

Figure 1. (A) ITA as a quantification of skin tone. (B) Participant distribution across ITAs (median ± range = 16.1 ± 106.7). Mean and median values shown in blue and red, and group boundaries in black.

2.2 Experimental design and tPBM protocol

Stimulation targeted the right prefrontal cortex (rPFC) using MDL-III lasers at 808 nm or 1064 nm delivering NIR light to a custom headpiece via a 400 µm fiber cable (**Figure 2a**) (Vielight Inc., Toronto, Canada). Each participant completed four EEG-tPBM recordings with distinct combinations of wavelengths (808 nm or 1064 nm), pulsation frequencies (10 Hz or 40 Hz), and irradiances (100, 150, or 200 mW/cm^2). Wavelengths of 808 nm and 1064 nm are widely used in tPBM studies due to their established tissue penetration and safety profiles, while 10-Hz and 40-Hz frequencies have demonstrated efficacy in prior studies (Zein et al., 2018). Three distinct protocols were created using the above parameter combinations (**Table 1**).

The number of participants per skin tone group per protocol was as balanced as possible. **Table 2** contains a list of tPBM dosage parameters. Each 12-min recording followed a PRE-DURING-POST design (4 minutes each) where the baseline (PRE) period served as a within-subject control in the absence of formal sham stimulation (**Figure 2b**). Parameters were controlled remotely and participants were blinded to the protocols and study design. Participants watched naturalistic stimulus videos to minimize drowsiness (Gal et al., 2022). No thermal sensations were reported. Moreover, a separate MR thermometry scan was performed to rule out intracranial thermal effects (see **Supplementary Materials** for details).

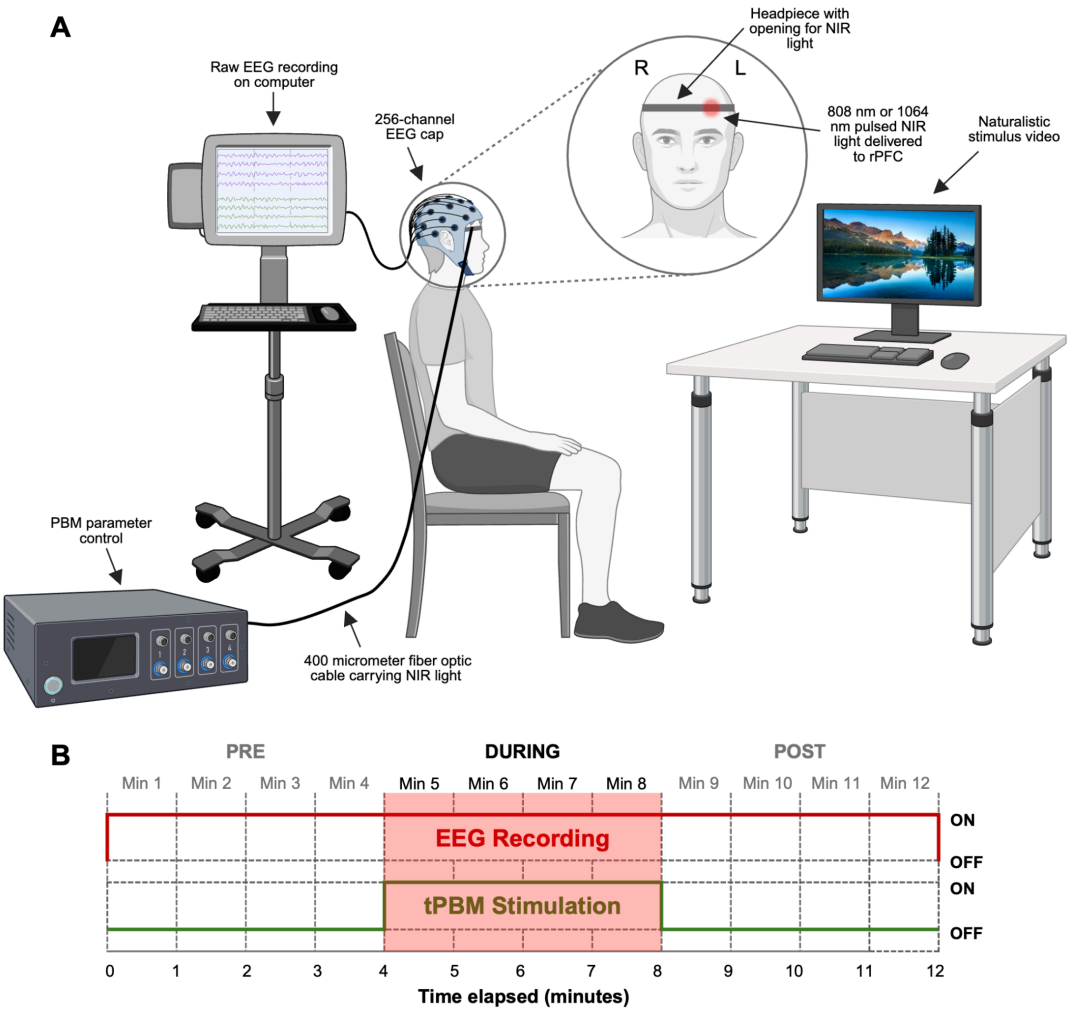

Figure 2. (A) Illustration of EEG-tPBM experimental setup created with BioRender.com. (B) EEG recording timeline following block stimulus design.

Table 1. Participant distribution across skin tone groups, protocols, sexes, and parameter values.

Skin Tone Group	ITA Range	Protocol 1	Protocol 2	Protocol 3	Total	M/F
Group 1	27° < ITA ≤ 55°	5	5	4	14	6 M / 8 F
Group 2	-1° < ITA ≤ 27°	6	5	6	17	9 M / 8 F
Group 3	ITA ≤ -1°	5	4	6	15	9 M / 6 F
Number of Subjects		16	14	16	46	24 M / 22 F
Number of Recordings		64	56	64	184	

Recording	Protocol 1	Protocol 2	Protocol 3
1	1064 nm, 100 mW/cm², 10 Hz	1064 nm, 150 mW/cm², 10 Hz	1064 nm, 150 mW/cm², 40 Hz
2	808 nm, 100 mW/cm², 10 Hz	808 nm, 150 mW/cm², 10 Hz	808 nm, 150 mW/cm², 40 Hz
3	1064 nm, 200 mW/cm², 10 Hz	1064 nm, 200 mW/cm², 40 Hz	1064 nm, 100 mW/cm², 40 Hz
4	808 nm, 200 mW/cm², 10 Hz	808 nm, 200 mW/cm², 40 Hz	808 nm, 100 mW/cm², 40 Hz
M / F	8 M / 8 F	7 M / 7 F	9 M / 7 F

Table 2. tPBM treatment parameters.

Parameter	Value
Duty cycle	50%
Beam spot size at stimulation site (cm^2)	≈ 1 cm^2
Wavelength (nm)	808 or 1064
Distance from scalp (cm)	~0
Pulsation frequency (Hz)	10 or 40
Irradiance at stimulation site (mW/cm^2)	100, 150, or 200
Duration of stimulation (minutes)	4
Radiant energy (J)	12.014, 18.021, or 24.028
Duty cycle	50%

2.3 EEG acquisition

EEG was recorded at 1,000 Hz with a 256-channel HydroCel Geodesic Sensor Net Amp 400 amplifier (Magstim Inc., Roseville, MN, USA) using saline electrodes (reference: Cz, <50 kΩ impedance, 0.024 µV amplitude resolution, 10-20 international placement system). A 20-minute break separated recordings to avoid potential carryover effects, which were studied at a later stage (see **Sec 2.4.3**). The data pipeline involved preprocessing, power analysis, and linear mixed-effect (LME) modeling (**Figure 3**).

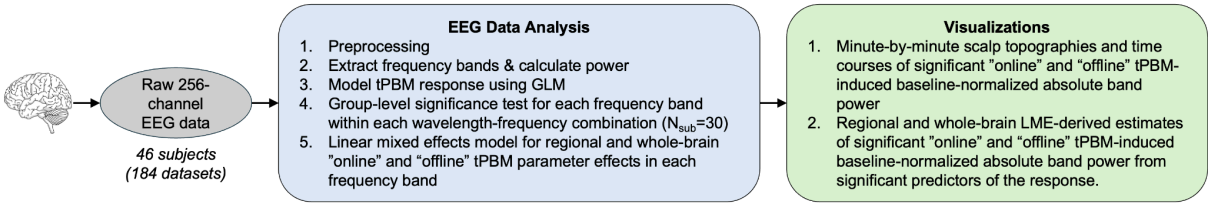

Figure 3. Summary of key stages in the data analysis pipeline.

2.4 EEG data analysis

2.4.1 Preprocessing

EEG data were processed using MATLAB (Mathworks Inc., Natick, MA, USA) with EEGLAB 2023.1. The preprocessing pipeline consisted of several sequential steps applied to each recording. The sixty-five face electrodes were disregarded in the 256-electrode array. Data were high-pass filtered at 1 Hz (to remove slow drifts while preserving delta activity) and downsampled to 125 Hz (providing adequate frequency resolution for low gamma analysis). Automated channel rejection was performed using the clean_rawdata algorithm with the following criteria: channels with <20% correlation to nearby channels were flagged as noisy (ChannelCriterion = 0.8), channels flat for >5 seconds were removed (FlatlineCriterion = 5), and line noise criterion was set to 4. This process excluded an average of 8.2 channels per dataset, yielding 182.8 channels across all preprocessed datasets. Independent Component Analysis (ICA) was performed using the extended infomax algorithm with automatic component ordering. Components were classified using ICLabel and those identified as eye movement artifacts, muscle activity, or line noise with probability>0.9 were automatically flagged and removed.

2.4.2 Frequency band extraction and power calculation

For each preprocessed dataset, EEG data were segmented into 1-minute non-overlapping epochs. Within each epoch, spectral power was estimated using Welch's method (60-second Hanning windows with 50% sliding-window overlap) to obtain robust power-spectral density estimates across canonical frequency-band ranges (delta: 1-4 Hz, theta: 4-8 Hz, alpha: 8-12 Hz, beta: 12-30 Hz, and low gamma: 30-50 Hz). Power spectral densities were integrated within each band to obtain absolute band power and baseline-normalized i.e. expressed as the percent change from the mean of pre-stimulation baseline (Min 1-4), shown in **Eq. 2**:

$$P_{norm}(t) = \frac{P_t - \overline{P_{1:4}}}{\overline{P_{1:4}}} \times 100 \qquad (2)$$

where P_{norm} is the baseline-normalized absolute power, P_t is the band power in minute t and $\overline{P_{1:4}}$ is the average band power over Min 1-4.

2.4.3 Identifying potential effects caused by EEG recording order

In order to confirm that the tPBM effects of earlier scans did not affect baseline EEG power in subsequent scans, we investigated whether baseline power was confounded by recording sequence. Linear mixed-effects (LME) models were applied to each frequency band, shown by **Eq. 3 and 4**:

Model 1: $\overline{PNorm_{6:8}} \sim 1 + Recording + (1 \mid Subject)$ (3)

Model 2: $\overline{PNorm_{6:8}} \sim 1 + Recording + (Recording \mid Subject)$ (4)

where $\overline{PNorm_{6:8}}$ is the average baseline-normalized absolute power in Min 6-8 (end of the DURING period), Recording is the recording index from 1-8, and Subject is the subject ID. Model comparison using likelihood-ratio tests (LRT) evaluated whether including random slopes for the recording improved fit and whether recording order predicted responses (see **Supplementary Materials**). P-values were FDR-corrected across bands.

2.4.4 Modeling the EEG response to tPBM with a generalized linear model

To capture plausible temporal profiles of tPBM-evoked EEG dynamics, two response regressors were defined to model expected changes during and after stimulation: (i) block regressor: a step function reflecting the OFF/ON/OFF stimulation ([0 0 0 0 1 1 1 1 0 0 0 0]) (ii) ramp regressor: a gradual increase beginning at stimulation onset and extending into the post-stimulation period ([0 0 0 0 $\frac{1}{8}$ $\frac{2}{8}$ $\frac{3}{8}$ $\frac{4}{8}$ $\frac{5}{8}$ $\frac{6}{8}$ $\frac{7}{8}$ 1]). The block regressor was motivated by past functional EEG studies of task response and the ramp regressor is motivated by the fact that past PBM studies have reported a ramp-like response in oxidated CCO (Saucedo et al., 2021; X. Wang et al., 2016). These vectors respectively modeled transient (step-like) and progressive-cumulative (ramp-like) patterns of power modulation expected during and after tPBM stimulation.

For each dataset, electrode e, and frequency band, the 12-minute baseline-normalized absolute power time courses, $P_e(t)$, were fit to both regressors using the generalized linear model (GLM) **(Eq. 5)**:

$$P_e(t) = \beta_e S(t) + \epsilon \qquad (5)$$

where S(t) was either the block or ramp regressor, β_e (slope) quantified how strongly the absolute power at electrode e followed the temporal profile, and ϵ was the residual error term.

2.4.5 Group-level significance testing of response temporal profiles

We next assessed which response profile (block or ramp) best characterized tPBM-induced power modulation. For each wavelength-frequency (WF) combination (808 nm and 10 Hz, 808 nm and 40 Hz, 1064 nm and 10 Hz, 1064 nm and 40 Hz, 30 subjects each; N_{sub}=30), and for each band and electrode, the following steps were performed:

1. Subject-specific β_e values were collected across recordings (if a subject underwent multiple recordings with the same WF combination).
2. An outlier-removed mean of β_e was computed across subjects.
3. A Wilcoxon signed-rank test (two-tailed, one-sample vs. 0) assessed whether the group-level median β_e differed significantly from 0.
4. P-values were corrected across electrodes using Benjamini-Hochberg false discovery rate (BHFDR; $q<0.05$) (Benjamini & Hochberg, 1995).
5. Electrodes meeting significance and a minimum-sample criterion ($\geq$15 subjects contributing data) were marked as significant and formed a significance mask for that band.

This process was performed separately for block- and ramp-based models. All subsequent analyses used significance masks from the regressor that demonstrated the most consistent group-level significance across WF combinations.

2.4.6 Topographies, time-courses, and regional/hemispheric analyses

For each wavelength-frequency combination, significance masks were used to display only significant FDR-corrected group responses to tPBM. Minute-by-minute scalp topographies and time courses show P_{norm} in Min 5-12 in each band. Values were first averaged within subjects across recordings with the same wavelength-frequency combination, then across subjects. To examine spatial patterns, each band's P_{norm} in Min 6-8 was further aggregated within scalp regions (prefrontal, frontal, central, parietal, temporal, occipital) and by hemisphere, based on electrode spatial coordinates.

2.4.7 Linear mixed effects modeling of tPBM parameter effects

To investigate the effects of tPBM parameters on P_{norm}, two analysis windows were defined: the end of the DURING (Min 6-8) and POST (Min 10-12) periods. For each dataset, the dependent variable Y was defined as P_{norm} averaged across electrodes for that window, yielding one value per dataset, frequency band, and analysis window. Then, two analyses were conducted: whole-brain, where Y was averaged across all electrodes, and regional, where Y was averaged across electrodes in each region.

Fixed effects (categorical unless noted) included primary tPBM parameters: wavelength (808/1064 nm), pulsation frequency (10/40 Hz), and irradiance (100/150/200 mW/cm^2) as well as biological covariates: sex (female/male) and ITA (continuous, z-scored skin tone index). Subject ID was included as a random intercept to account for inter-subject variability across repeated recordings.

For each band×time window (and each region in the regional analysis), a hierarchy-respecting, exhaustive model search was performed to identify the optimal fixed-effects structure. All main effects were included, and all possible two-way interactions were tested, provided their constituent main effects were present. Models were fit using maximum likelihood (ML), and the best model was selected based on the lowest Bayesian Information Criterion (BIC). The winning model was refit using restricted maximum likelihood (REML) for inference. A minimum of 10 datasets was required for model estimation; band × window × region combinations below this threshold were excluded. For each final model, fixed-effect estimates and 95% confidence intervals (CIs) were obtained, and p-values for non-intercept effects were FDR corrected (BHFDR; $q<0.05$). Only FDR-significant effects were visualized.

3 RESULTS

3.1 Ramp regressor better modeled tPBM-induced power responses

For the block-shaped regressor, no significant modulations in P_{norm} were found at the group level (after FDR correction), for any band, in any wavelength-frequency grouping.

There were, however, significant responses to the ramp-shaped responses and, interestingly, all electrodes showed $\beta>0$, implying no decreasing trends at the group-level. This suggests that in our window of measurement, tPBM was associated with progressive and cumulative increases and not decreases in P_{norm} at the group level. As a result, subsequent results and visualizations were generated from significant electrodes identified by the ramp-based model.

Within each wavelength-frequency combination, P_{norm} demonstrated interesting online (DURING) and offline (POST) responses to tPBM and we will describe these separately. Although a ramp response can be observed in each group, especially in beta and gamma bands (**Figure 4-5**), it differed with the pulsation frequency used and also across frequency bands.

3.2 tPBM's online effect on EEG power

Figure 4 summarizes the outcome of the group analysis (ramp regressor) for the 808 nm wavelength-frequency combinations. With 808 nm-10 Hz (**Figure 4a**), the baseline-normalized absolute power maps show that the online response displayed subtle decreases in the delta band, moderately increased in the occipital theta band, and was not significantly modulated in the alpha band. then progressively increased in the beta and gamma bands, with gamma displaying the strongest increases toward the end of the online period. Using 808 nm-40 Hz (**Figure 4b**), similar trends are observed, with the increases in the beta and gamma bands more substantial than 40-Hz. As the time course plots show, the 10-Hz condition seems to result in a steady, growing increase during the course of the stimulus and beyond, while the 40-Hz beta and gamma time courses begin to plateau before declining (**Figure 4b**).

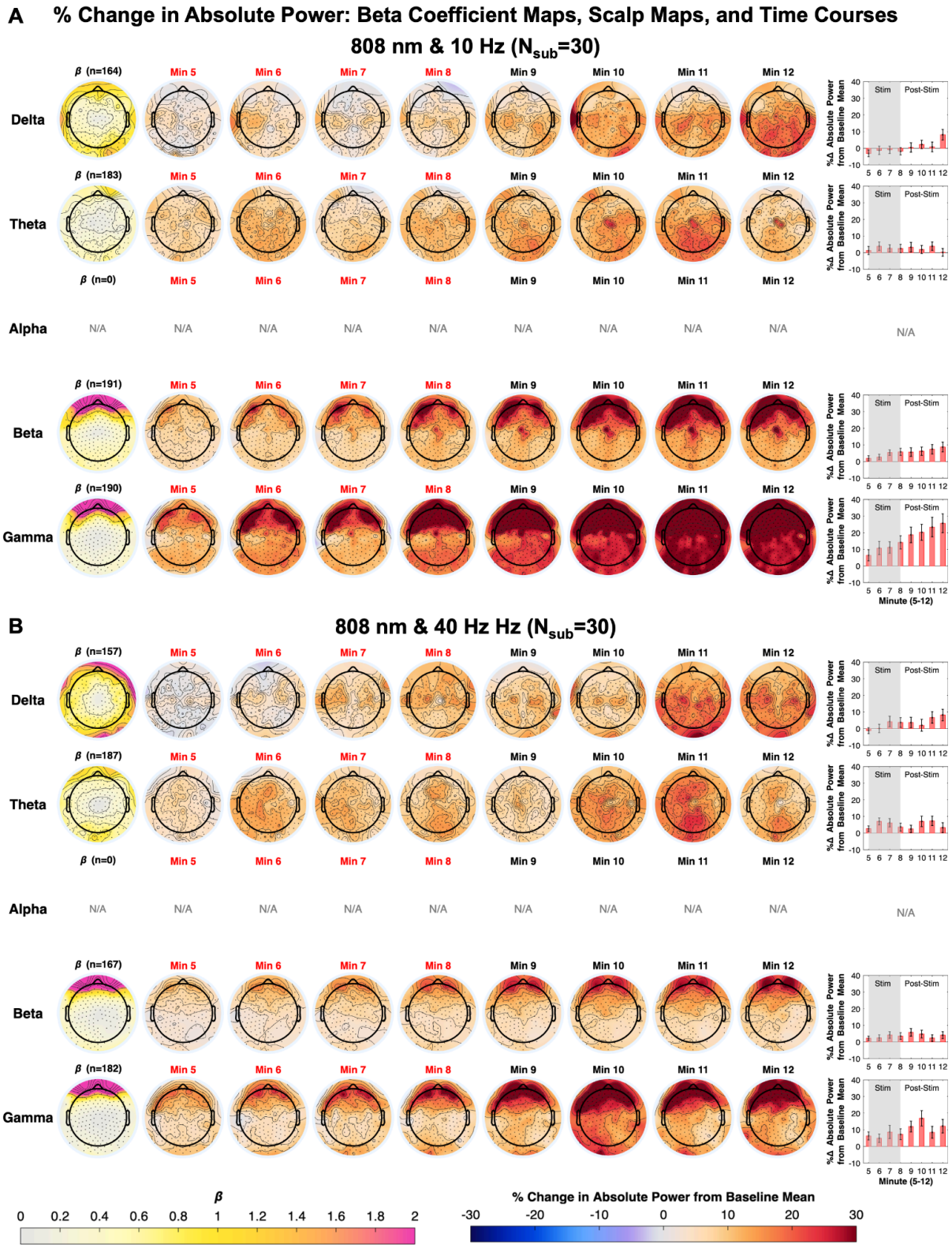

Figure 4. Baseline-normalized absolute band power follows a ramp-like response to 808-nm tPBM. (A) 10 Hz; (B) 40 Hz. Column 1: group-level β-coefficient maps (ramp regressor) plotting electrodes with FDR-significant β values (electrode counts *n* shown above the maps). Columns 2 to 9: group-level scalp topographies of percent change in absolute power for the *n* electrodes, baseline-normalized to Min 1-4, for Min 5-12. Column 10: group-level time courses using data from the *n* electrodes (N_{sub}=30; mean ± error bars for inter-subject variability).

Figure 5 displays the group-level analysis results for the wavelength-frequency combinations for the 1064-nm wavelength**. Figure 5a** shows that, with the ramp regressor, significant electrodes were identified (all $\beta>0$) in all bands except delta and alpha. Among these electrodes, the increase in power was moderate and modest in the theta band, with the most pronounced increases found in the beta and gamma bands, as before. As shown in **Figure 5b**, for the 1064 nm-40 Hz combination, significant electrodes were identified (all $\beta>0$) in all bands except alpha and we actually observe an online response pattern almost identical to that of the 808 nm-10 Hz combination **(Figure 4a)**. In this case, however, the beta response remained local throughout most of the stimulation period, becoming more global close to the end of stimulation and into the recovery period. Gamma responses, on the other hand, increased over time and also started propagating towards posterior areas in the first minute of stimulation, growing as stimulation progressed as well as into the post-stimulation period.

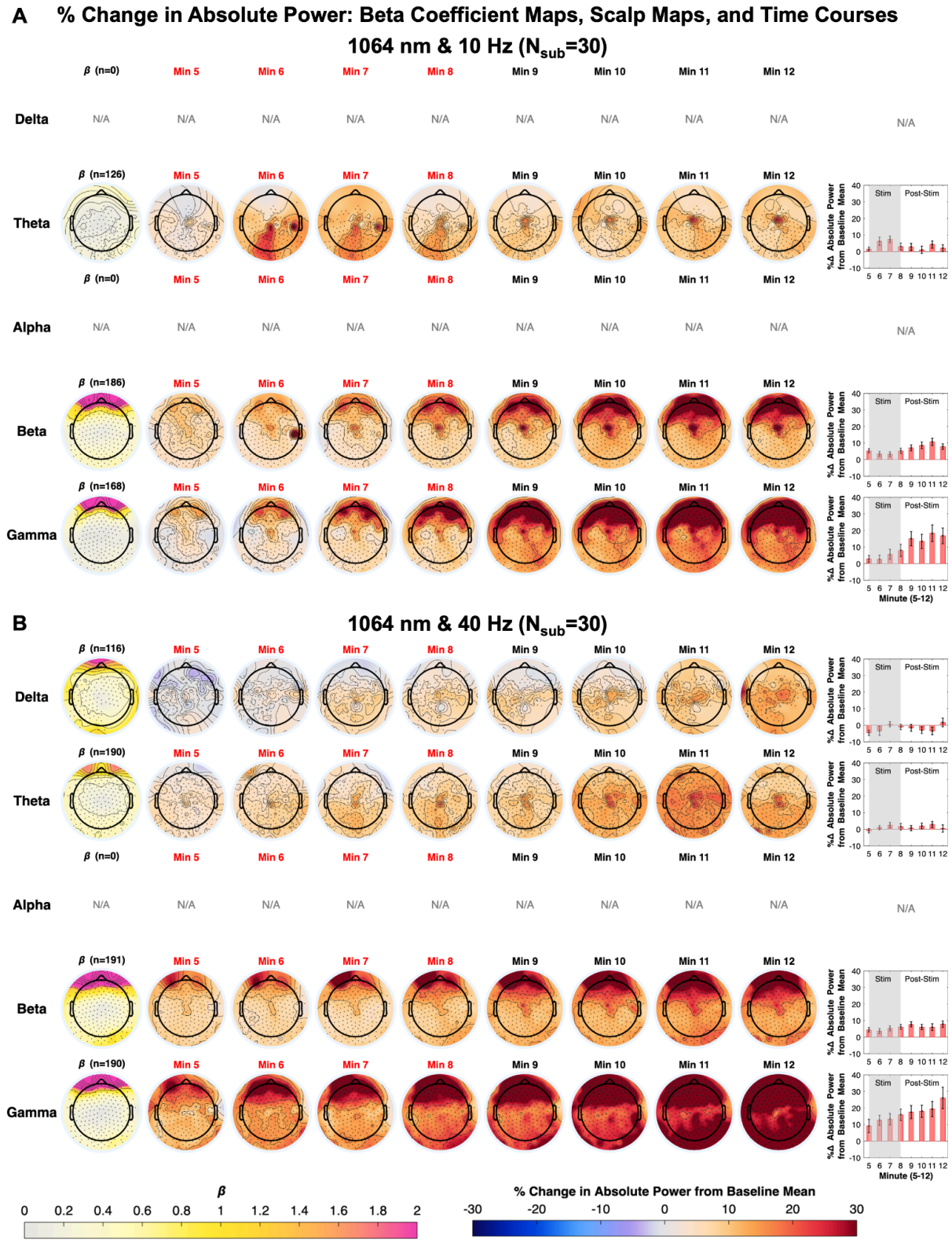

Figure 5. Baseline-normalized absolute band power follows a ramp-like response to 1064-nm tPBM. (A) 10 Hz; (B) 40 Hz. Column 1: group-level β-coefficient maps (ramp regressor) plotting electrodes with FDR-significant β values (electrode counts *n* shown above the maps). Columns 2 to 9: group-level scalp topographies of percent change in absolute power for the *n* electrodes, baseline-normalized to Min 1-4, for Min 5-12. Column 10: group-level time-courses using data from the *n* electrodes (N_{sub}=30; mean ± error bars for inter-subject variability).

Figure 6a summarizes the topography maps for the 808 nm combinations (**Figure 4a)** and shows us that in the delta band, the power response to 808 nm-10 Hz was very minimal close to the point of stimulation, the rPFC, and was actually highest around the middle of the brain, the central, parietal, and temporal regions (**Figure 6a**), consistent with the maps in **Figure 4a**. In the theta band, we see a stronger response near the rPFC, with the response increasing in regions further away from the stimulation site. In the beta and gamma bands, we see the opposite pattern: the response was highest in the prefrontal region and decreased in strength in regions further away from the rPFC. **Figure 6b** displays a very similar pattern to **Figure 6a** however, the regional responses in the beta and gamma bands appear weaker when using 808 nm pulsed at 40Hz (**Figure 6b**) than 10 Hz (**Figure 6a**), although the propagation of the response between the regions remained the same. This same spatial pattern is also observed in the scalp maps and time courses (**Figure 4**). **Figure 6c** shows us that when using 1064 nm-10 Hz, the regional pattern of band power increases are the same as in **Figure 6b**, using 808nm-40 Hz, except there was no significant delta power modulation with 1064 nm-10 Hz. This remains consistent with the online spatial patterns shown in the scalp topographies (**Figure 4b and 5a**). Interestingly, just like how the power response to 1064 nm-10 Hz matched that of the 808 mn-40 Hz, **Figure 6d** tells us that the response to 1064 nm-40 Hz matches that of 808 nm-10 Hz. We see a similar pattern of response propagation through the brain regions, but this time the gamma response was strongest using 1064 nm-40Hz, again aligning with the spatial patterns from **Figure 5b**.

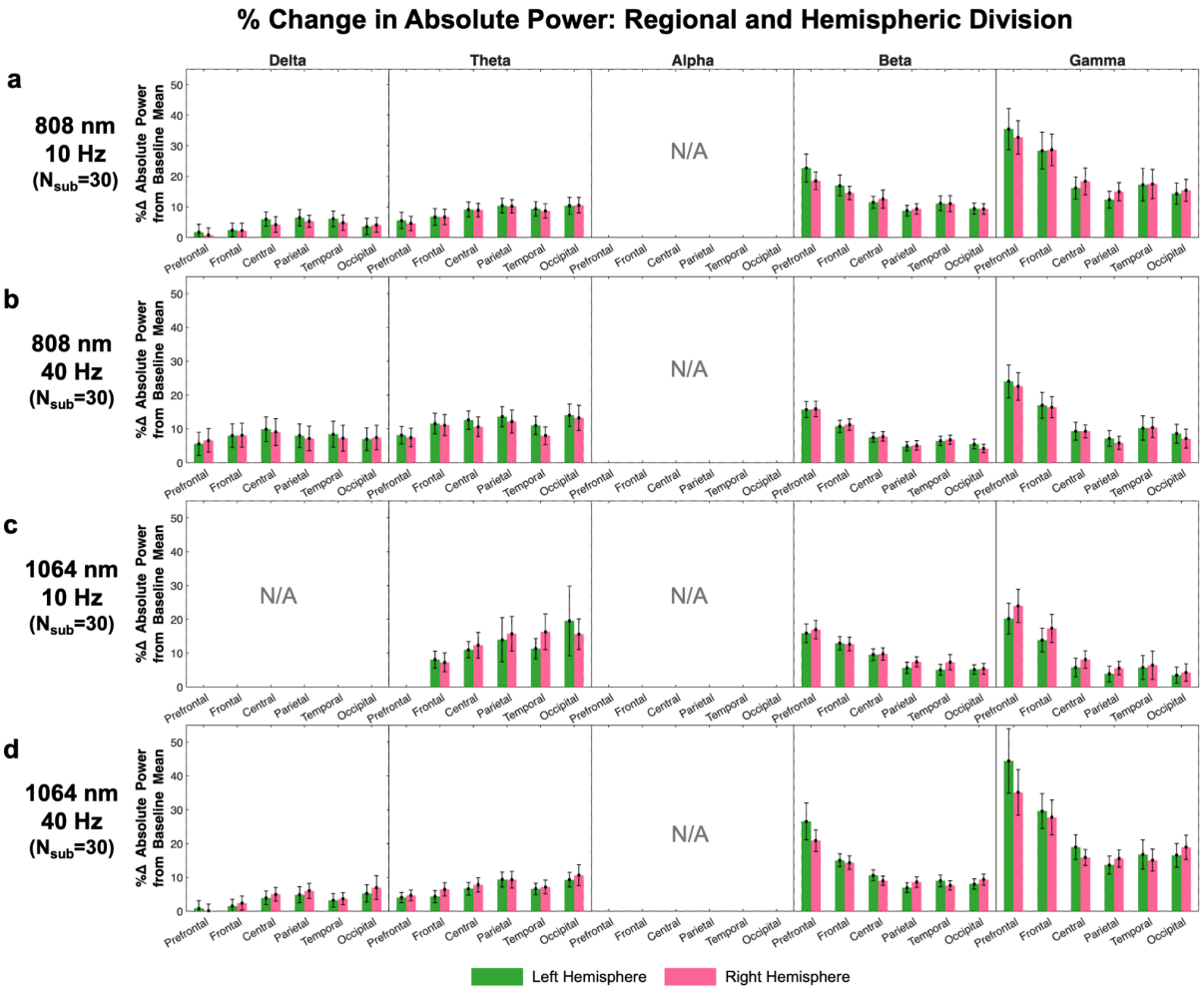

Figure 6. Regional and hemispheric baseline-normalized absolute band power response to tPBM in Min 6-8. (A) 808 nm-10 Hz; (B) 808 nm-40 Hz; (C) 1064 nm-10 Hz; (D) 1064 nm-40 Hz. Bars show mean ± error bars for inter-subject variability of percent change in absolute power, baseline-normalized to Min 1-4, averaged over Min 6-8 and over significant electrodes within each region and hemisphere.

3.3 tPBM's offline effect on EEG power

Although the online responses to tPBM revealed interesting wavelength-frequency coupling dynamics, the offline period captured heightened responses. **Figure 4** shows all bands, except alpha, displaying a persistent power increase up to Min 12. Theta and gamma power modulation showed recovery at Min 11 for 808 nm-10 Hz, but gamma showed recovery at Min 10 for 808 nm-40 Hz.

Figure 5 shows that in both 1064 nm-10 Hz and 40 Hz conditions, there were mild theta power increases persisting into the recovery period, especially in Min 11 with 1064 nm-40 Hz. Although there was no significant alpha modulation, we observe prolonged beta and gamma power increases until the end of Min 12. Overall, the offline response to 1064 nm-10 Hz looks similar to that of 808 nm-40 Hz (**Figure 5a**), whereas the offline response to 1064 nm-40 Hz resembles that of 808 nm-10 Hz, with some differences.

3.4 tPBM parameter effects on baseline-normalized EEG responses

Figure 7 shows two forest plots of FDR-corrected significant ($q<0.05$) LME-derived estimates of baseline-normalized absolute power responses in the whole-brain (**Figure 7a**) and regional (**Figure 7b**) analyses. These dependencies in tPBM's online and offline effects are summarized in **Table 3** and **Table 4** respectively.

Table 3. Parameter effects on the tPBM-induced online baseline-normalized EEG power responses.

		Alpha	**Beta**	**Gamma**
Wavelength			**Larger** for 808 nm than 1064 nm in the temporal region.	**Larger** for 808 nm than 1064 nm, especially in the frontal, central, parietal, temporal, and occipital regions.
Frequency	*Independent*			**Larger** for 10 Hz than 40 Hz in the parietal region.
	Wavelength interaction		**Larger** for 40 Hz than 10 Hz, at 1064 nm, especially in temporal and occipital regions.	**Larger** for 40 Hz than 10 Hz, at 1064 nm across all regions.
Irradiance			**Larger** for 150 mW/cm^2 than 100 mW/cm^2, especially in prefrontal, frontal, central, and temporal regions.	**Larger** for 150 mW/cm^2 than 100 mW/cm^2, especially in prefrontal, frontal, central, parietal, and temporal regions.
Skin tone		**Larger** for lighter skin in the prefrontal region.		**Larger** for lighter skin in central, parietal, and occipital regions.

Table 4. Parameter effects on the tPBM-induced offline baseline-normalized EEG power responses.

		Delta	Alpha	Beta	Gamma
Wavelength				**Larger** for 808 nm than 1064 nm in the occipital region.	
Frequency	*Independent*			**Larger** for 10 Hz than 40 Hz in the temporal region.	
	Wavelength interaction			**Larger** for 40 Hz than 10 Hz, at 1064 nm, especially in temporal and occipital regions.	**Larger** for 40 Hz than 10 Hz, at 1064 nm, especially in central, parietal, and occipital regions.
Irradiance			**Larger** for 150 mW/cm^2 than 100 mW/cm^2 in prefrontal, frontal, central, parietal, and occipital regions.	**Larger** for 150 mW/cm^2 than 100 mW/cm^2, especially in the temporal region.	
Skin tone	*Independent*		**Larger** for lighter skin in the prefrontal region.		
	Sex interaction		**Larger** for darker skin in the prefrontal region, in males.		
Sex	*Independent*	**Larger** for females than males in the central region.		**Larger** for females than males in the occipital region.	
	Wavelength interaction		**Larger** for males than females, at 1064 nm, especially in the prefrontal region.	**Larger** for males than females, at 1064 nm, especially in the occipital region.	
	Frequency interaction	**Larger** for males than females, at 40 Hz, in the central region.			

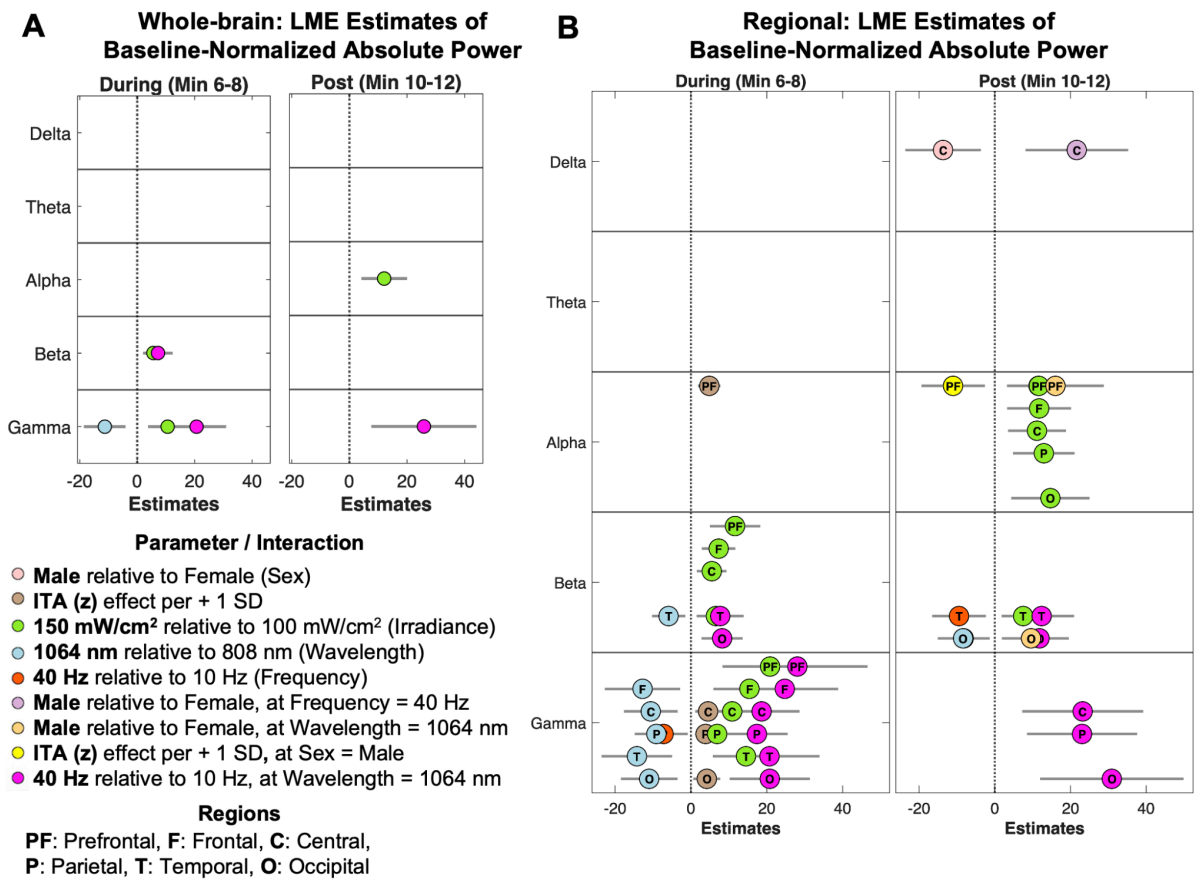

Figure 7. LME-derived estimates of baseline-normalized absolute band power during and post-tPBM. (A) whole-brain and (B) regional LME models showing fixed-effect estimates (±95% CIs as grey lines) for significant predictors of power changes across frequency bands. Models were fit separately for DURING (Min 6-8) and POST (Min 10-12) windows using baseline-normalized absolute power averaged in each band. Each colored point denotes a parameter or interaction term that significantly contributed to explaining variance in the dependent variable after BHFDR correction ($q<0.05$). Categorical effects (wavelength, frequency, irradiance, sex) are expressed relative to their reference levels (808 nm, 10 Hz, 100 mW/cm^2, female), while continuous covariates (ITA) represent effects per + 1 SD. Interaction effects are interpreted as the modulation of one parameter's effect at the other fixed level. Acronyms on the markers correspond to brain regions.

4 DISCUSSION

Our study aimed to characterize how tPBM targeting the right forehead modulates EEG activity in real-time in healthy young adults. We show, for the first time, that (i) tPBM induces significant and cumulative increase in neural oscillatory power that persisted beyond the stimulation period; (ii) these temporal and spatial response patterns are frequency-band-dependent; (iii) power responses start at the irradiation site and spread across the brain over a period of >4 min. Parameter comparisons reveal that (iv) the 808-nm wavelength and 150-mW/cm^2 irradiance consistently produced larger alpha/beta/gamma responses compared to 1064 nm and 100 mW/cm^2, respectively (with no significant difference between 100 and 200 mW/cm^2), (v) pulsation frequency and sex effects were laser-parameter-dependent, and finally, (vi) lighter skin was linked to larger responses. Our findings address a critical gap in the current literature by providing new insights on the temporal and spatial progression of tPBM's effect during and after stimulation with varying parameters.

4.1 Cumulative and sustained tPBM-induced EEG response

Across all tested laser-parameter combinations, we found significant group-level tPBM-induced increases in baseline-normalized absolute power, P_{norm}, that appeared cumulative throughout the stimulation period (online) and persisting for several minutes post-stimulation (offline). These effects were evident in all bands except alpha and were particularly strong in gamma, followed by beta. Delta/theta changes were smaller and more variable (**Figures 4-5**). However, unlike previous studies (X. Wang et al., 2019) in which the EEG response returned to baseline fairly shortly after stimulation cessation, our study is the first to formally demonstrate a cumulative EEG-power response that not only evolves during the stimulus period but remains for the entire 4-minute post-stimulus period. Our findings of beta elevation align with those of Zomorrodi et al. who targeted the DMN using 810-nm tPBM (with intranasal) pulsed at 40 Hz for 20 minutes (Zomorrodi et al., 2019). Various other studies employing continuous tPBM at 1064-nm targeting the rPFC (Pruitt et al., 2024; Shahdadian et al., 2022; X. Wang et al., 2019, 2021) present a similar response pattern, with eyes open (Shahdadian et al., 2022; X. Wang et al., 2019, 2021) and eyes-closed (Shahdadian et al., 2022; X. Wang et al., 2021) protocols. Notably, during 11 minutes of tPBM stimulation, Wang et al. reported progressive increases in alpha/beta power, with the highest increases near the end of the stimulation window (X. Wang et al., 2019). Similar findings pertain to a study with 8-min tPBM (X. Wang et al., 2021). Shahdadian et al. showed a mirroring similar response in delta power, which progressively decreased (Shahdadian et al., 2022), which mimics our delta responses in the 808-nm conditions.

These temporal dynamics may reflect the cellular effects of tPBM. It is well-established that the photoexcitation of CCO by NIR light increases mitochondrial oxidative phosphorylation and ATP availability (de Freitas & Hamblin, 2016; Wong-Riley et al., 2005). In active neural circuits, the majority of this ATP is taken up in powering Na^+/K^+ ion pumps that restore ionic gradients between subsequent postsynaptic currents and action potentials (Attwell & Laughlin, 2001; Harris & Attwell, 2012; Theriault et al., 2023). At the scalp level, these more robust postsynaptic currents manifest as higher beta/gamma band power (Nunez and Srinivasan, 2005; Thut et al., 2012). An increase in ATP availability enhances the ability of neurons, especially fast-spiking interneurons, to maintain rapid, rhythmic firing, characteristic of beta and gamma bands. The cumulative appearance of this effect might reflect the build-up and gradual dissipation of these metabolic changes, rather than any continuing photonic influence. Notably, our cumulative sustained EEG responses are more consistent with the previous fNIRS results that also showed a cumulative increase in both the concentration of oxidated CCO and oxy-hemoglobin (Saucedo et al., 2021). This is consistent with the fact that high-frequency, metabolically expensive rhythms require hyperemia to sustain (Drew, 2022; Howarth et al., 2012; Moore & Cao, 2008), potentially bridging downstream sustained effects to neurovascular coupling through NO-mediated vasodilation via PBM's photodissociation of NO from CCO (Hosford and Gourine, 2019; Yan et al., 2025) (see **Sec 4.4.1**).

4.2 EEG response is dominated by beta/gamma power increases

We found that tPBM modulated P_{norm} in higher-frequency (beta/gamma) bands more than it did in low-frequency (delta/theta) bands. In previous EEG-tPBM studies, the definition of the gamma band varied considerably: 30-50 Hz (Zomorrodi et al., 2019), 30-70 Hz (X. Wang et al., 2019, 2021), 31-80 Hz (Pruitt et al., 2024), 30-70 Hz (Shahdadian et al., 2022), 30-55 Hz (Spera et al., 2021). Notably, only studies that used a narrower low-gamma window of 30-50/55 Hz (Spera et al., 2021; Zomorrodi et al., 2019), similar to ours, reported significant increases in gamma power. While this higher-frequency power enhancement remains consistent with findings from healthy adults (Pruitt et al., 2024; X. Wang et al., 2019, 2021; Zomorrodi et al., 2019), the emphasis of the beta, and especially gamma, bands appear unique to our study.

This higher-frequency predominance is likely attributed to the distinct metabolic demands of the beta and, specifically low-gamma, rhythms. Beta activity is commonly associated with executive control and top-down regulation (Engel & Fries, 2010; Gola et al., 2012; Miller et al., 2018; Palacios-García et al., 2021; Schmidt et al., 2019), while gamma oscillations arise from rapid interactions between excitatory pyramidal neurons and fast-spiking GABAergic interneurons (Buzsáki

and Wang, 2012; Fernandez-Ruiz et al., 2023; Kann et al., 2014; Traub, 2000). These microcircuits depend on fast cycles of voltage-gated Na^+, K^+, and Ca^{2+} channels and sustained excitatory-inhibitory synaptic transmission, both of which are energetically expensive (Kann, 2011; Kann et al., 2014). Due to these energy demands, higher-frequency power tends to increase with sensory drive and cognitive engagement, rising when neurons are strongly driven by input or attention (Manyukhina et al., 2021; Miller et al., 2018; Stroganova et al., 2015; van Kerkoerle et al., 2014) and falling in metabolically constrained conditions (Fano et al., 2007; Kann, 2011; Pietersen et al., 2009; Whittaker et al., 2011). This metabolic sensitivity suggests that high-frequency rhythms are constrained by the availability of ATP needed to restore ionic gradients. Within this framework, the tPBM-induced enhancement of beta/gamma activity may indicate a shift toward a higher level of ATP availability, as mentioned earlier. This is consistent with the widely reported cognitive improvements in response to tPBM (Barrett & Gonzalez-Lima, 2013; Chan et al., 2019; Shen et al., 2024; Tang et al., 2023; Vargas et al., 2017).

On the other hand, delta/theta rhythms reflect slower, larger-scale fluctuations in network excitability that are less dependent on ATP availability. Delta activity dominates during slow-wave sleep, where it supports memory consolidation and glymphatic clearance (Léger et al., 2018; Reddy & van der Werf, 2020), and can briefly appear during quiet wakefulness when inhibitory control systems transiently disengage (Harmony, 2013; Sachdev et al., 2015). In contrast, theta activity supports memory and attentional processes (Herweg et al., 2016; Karakaş, 2020; Klimesch, 1999; Klimesch et al., 2001), but at rest it typically reflects a baseline level of cognitive readiness rather than active processing. As these slower rhythms do not require the levels of rapid ion-channel cycling or sustained synaptic firing needed to support higher-frequency rhythms, they are not as affected by the cell's immediate ATP supply. In awake, eyes-open resting states, as in our experiment, the brain would naturally occupy a moderately alert state with relatively low delta/theta activity. Thus, the weaker modulation of these low-frequency bands we observe may simply reflect that tPBM is not pushing the brain further into a sleep-like or disengaged state, but instead is supporting high-frequency processes that underlie cortical activation and information integration.

Moreover, the lack of significant group-level alpha power modulation in our data could be attributed to the use of this specific resting state. Since alpha power is known to increase in eyes-closed resting states, to mitigate drowsiness and regulate the brain state, participants in our study watched naturalistic stimulus videos throughout EEG-tPBM recordings. This likely reduced alpha participation and responsiveness. In fact, Spera et al. also reported no significant alpha responses (only beta/gamma) in their eyes-open condition after pulsed tPBM (Spera et al., 2021).

4.3 EEG response propagated spatially from front to back of the brain

Despite shining the laser on a small 1 mW/cm^2 area on each participant's right forehead, we observe significant changes in P_{norm} across the brain. These changes began near the irradiation site (rPFC) and spread to posterior brain regions over a period of more than four minutes. This spatial propagation was consistent in all responding frequency bands and, in most parameter combinations, appeared fastest in beta/gamma bands. While past studies using continuous tPBM have also reported certain spatial propagations in the EEG response (Pruitt et al., 2024; Shahdadian et al., 2022; X. Wang et al., 2019), in most cases the EEG responses set in immediately, and the spatial propagation was limited. Our study is the first to show the gradual and clear anterior-to-posterior spread of tPBM's EEG response stemming from the stimulation site. This propagation is important for understanding the mechanisms of tPBM in brain therapy.

This spatial pattern could reflect the interconnectedness of nearby brain regions rather than the physical spread of light. The rPFC has dense corticocortical connections to various brain regions (Haber and Robbins, 2022), and better metabolic support for neuronal circuits sustained by beta/gamma rhythms may facilitate propagation of the stimulus. This propagation has been observed in other brain-stimulation paradigms such as transcranial magnetic stimulation (Bashir et al., 2020; Nahas et al., 2001; J. B. Wang et al., 2024). Glial networks may further facilitate this spatial spread as astrocytes share extensive networks spanning broad cortical areas (Nortley & Attwell, 2017), regulating local extracellular ions and supplying energy substrates to neurons (Allen, 2014; Nortley & Attwell, 2017). They also release ATP via calcium-dependent mechanisms that can modulate local neuronal

excitability (Illes et al., 2019). However, this network-centric hypothesis does not rule out alternative mechanisms, such as biophoton release.

Biophoton signaling pathways between neurons have been reported (Grass et al., 2004; Mothersill et al., 2019; Salari et al., 2015; Tang and Dai, 2014; Van Wijk et al., 2020; Zangari et al., 2021). Neurons and glia can emit ultra-weak photons, which may be absorbed by chromophores within neighboring cells, including CCO, and could influence electrical activity or metabolic state through redox-sensitive mechanisms. As tPBM uses external photons that interact with similar chromophores involved in biophoton processes, some authors have proposed that PBM may engage or amplify the brain's endogenous biophoton network (Hamblin, 2016; Liebert et al., 2014). Under this hypothesis, tPBM-induced changes in mitochondrial states could momentarily increase biophoton emission, which might then influence nearby or connected neurons through photonic absorption. While its functional significance is not yet established, biophoton signaling could in principle contribute an additional pathway for distributing tPBM-induced changes across broader cortical regions.

4.4 Parameter dependencies in the EEG response

4.4.1 Wavelength-dependent cellular mechanisms: 808 nm vs. 1064 nm

The wavelength of NIR light used in tPBM strongly influences how deeply photons penetrate the skull and which intracellular structures absorb them, thereby shaping both the magnitude and spatial distribution of EEG responses (Zein et al., 2018). Monte Carlo simulations, including those from our group (Van Lankveld et al., 2025), indicate that the 810-nm wavelength produces significantly higher fractional energy deposition in the cortex than 1064 nm, in agreement with previous simulation work (Cassano et al., 2019; Li et al., 2017). Across age groups and brain regions, 808/810 nm tends to yield the highest effective dose at the cortical tissue, with 1064 nm typically emerging as the next most effective wavelength (Yuan et al., 2020). Accordingly, in our LME results, the shorter 808-nm wavelength consistently elicited larger beta/gamma power increases during tPBM compared to 1064 nm, with other parameters held at reference values (10 Hz, 100 mW/cm^2, female, lighter skin).

At the cellular level, these dosimetric differences are complemented by the distinct absorption profiles of key chromophores like CCO, which exhibits prominent absorption peaks in the red and NIR range; a relative maximum around ~810 nm and markedly reduced absorption at longer wavelengths (Hamblin, 2018; Hennessy and Hamblin, 2017; Oron et al., 2007; Salehpour et al., 2018; X. Wang et al., 2017). Therefore, 808/810 nm NIR light may be more efficiently absorbed by CCO, allowing it to photodissociate from inhibitory NO to bind with oxygen, supporting stronger mitochondrial activation, oxygen consumption, ATP synthesis, and reduced oxidative stress (de Freitas & Hamblin, 2016; Wong-Riley et al., 2005). By increasing ATP production, tPBM could raise the energetic "ceiling" that supports fast, metabolically costly oscillations like beta/gamma, offering a plausible explanation for the sustained higher-frequency band effects observed in our data.

In contrast, 1064 nm light is closer to the absorption spectrum of water (Lyu et al., 2022; Salehpour et al., 2018; Sandell and Zhu, 2011), especially relevant in forehead delivery where light must traverse the cerebrospinal fluid (CSF), leading to attenuated photon availability and less light reaching mitochondrial CCO. That said, 1064-nm light may engage with water-mediated and thermally sensitive mechanisms more, such as the activation of heat- and light-gated ion channels (Sharma et al., 2023), part of the transient receptor potential (TRP) channels. When water molecules absorb these higher NIR wavelengths, energy is converted to heat through molecular vibrations leading to local rapid temperature rises that gate heat-sensitive TRP calcium channels and/or change membrane capacitance, driving calcium ion influence and neuronal excitability (Liebert et al., 2023; Shapiro et al., 2017; Sharma et al., 2023).

Taken together, current dosimetry and cellular evidence suggest that 808 nm is particularly well-suited for promoting high-frequency brain oscillations. However, optimal wavelengths may still fail to produce meaningful biological effects if not paired with other appropriate dosing parameters such as pulsation frequency and irradiance, which combine to determine the amount and manner in which energy is being supplied to cortical tissue.

4.4.2 Pulsation frequency matters: 10 Hz vs. 40 Hz and their wavelength interactions

While our data revealed significant differences in the cortical response to 10-Hz and 40-Hz tPBM, these effects were strongly shaped by wavelength. As shown in **Figure 7**, the 808-nm wavelength with 10-Hz pulsing corresponded to larger gamma responses in the parietal region than 40 Hz, whereas 1064 nm with 40-Hz pulsing produced larger beta especially in temporal and occipital regions) and larger gamma responses (across all regions). Post-tPBM, 808 nm at 10 Hz led to larger beta responses in the temporal region, while 1064 nm at 40 Hz resulted in larger temporal and occipital as well as larger central, parietal and occipital gamma responses. These results align with the scalp topographies that show the 808 nm-10 Hz and 1064 nm-40 Hz combinations producing larger beta/gamma power increases, suggesting frequency-dependent resonance or entrainment effects (Kim et al., 2017; Tang et al., 2023) characterized by wavelength-specific mechanisms.

From a biophysical perspective, pulsed stimulation offers several advantages over continuous irradiation, including brief recovery intervals between pulses, reduced thermal buildup, and the potential to interact with intrinsic neural oscillations through frequency matching (Gillespie et al., 2017; Hashmi et al., 2010; Kim et al., 2017). As discussed earlier, at 808 nm, photon absorption by CCO is near its spectral maximum and therefore, pulsing at 10 Hz could match the cycles of photoexcitation and recovery that allow efficient mitochondrial activation without saturation or overheating. Consistent with this, while studying wound healing in rats, Keshri et al. reported that 810-nm light with 10-Hz pulsing produced the highest CCO activity, ATP synthesis, and cellular proliferation (compared to continuous and 100-Hz pulsing) while downregulating inflammatory mechanisms and upregulating angiogenetic processes (Keshri et al., 2016), suggesting that pulsing at this frequency may be optimal for CCO-mediated mitochondrial dynamics. Conversely, since 1064-nm light interacts more weakly with CCO and more strongly with water and gated ion channels, these microthermal oscillations likely activate thermosensitive TRP channels and alter membrane capacitance (Sharma et al., 2023) in a cycle more closely aligned with the 40-Hz rhythms. This could be the reason we see 40-Hz pulsing producing larger beta/gamma responses than 10-Hz using 1064 nm.

Among other EEG-tPBM studies, our strong gamma modulation aligns most closely with that shown by Zomorrodi et al., whose pulsed 40-Hz delivery also enhanced gamma power (Zomorrodi et al., 2019). By contrast, Spera et al. did not detect significant gamma effects under 830 tPBM pulsed at 10 Hz (Spera et al., 2021), even though our 808 nm-10 Hz results did, likely because their irradiance (54.8 mW/cm^2) was markedly lower than ours (100-200 mW/cm^2), suggesting a dose-dependent effect (see **Sec 4.4.3**). Similarly, in a continuous versus pulsed comparison, Tang et al. reported significantly higher gamma power during 850-nm tPBM, compared to baseline, only with pulsed 40-Hz delivery, not continuous (Tang et al., 2023). Altogether our findings add to the rationale that both 10-Hz and 40-Hz pulsing can be used to modulate high-frequency EEG power, and not just to target their corresponding frequency range of alpha and gamma, respectively. However, our results highlight that the choice of frequency should be dependent on wavelength.

Beta, and particularly gamma, rhythms require sustained, high-rate ion channel cycling and interneuron firing, processes that impose substantial ATP and oxygen requirements (Kann, 2011). Experimental work has shown that gamma oscillations are among the first to collapse under metabolic stress, such as brought about by hypoxia (Fano et al., 2007; Pietersen et al., 2009) or mitochondrial inhibition, including at CCO (Kann et al., 2011; Whittaker et al., 2011) and that their power correlates strongly with oxygen consumption (Kann et al., 2011) and $CMRO_2$ (Niessing et al., 2005). Therefore, increases in resting-state beta/gamma power following tPBM could reflect an improved neuroenergetic environment, one in which mitochondrial photostimulation increases ATP synthesis capacity and oxygen utilization efficiency, thereby sustaining fast oscillatory dynamics. This interpretation complements our 808-nm tPBM results, which produces the largest beta/gamma increases likely via enhanced CCO activation.

These findings reveal that pulsation frequency is a critical tPBM parameter that influences high-frequency oscillations, especially gamma, and may directly affect the brain's energy ceiling, enabling or maintaining high-frequency synchronization across cortical networks. Clinically, this is especially relevant for neurodegeneration, since 40-Hz stimulation has demonstrated the ability to modulate gamma rhythms for treating AD pathology (Blanco-Duque et al., 2024; Cardin et al., 2009;

Iaccarino et al., 2024; Park and Tsai, 2025) and strengthening cognition (Blivet et al., 2025; Chen et al., 2025; Liu et al., 2022).

4.4.3 Irradiance and biphasic dose responses

Irradiance, or optical power density, is arguably the most important determinant of tPBM efficacy and safety (Zein et al., 2018). In our study, irradiance significantly modulated the strength of EEG responses, keeping other parameters at reference values (808 nm, 10 Hz, female, lighter skin). This was in part predicted by Monte Carlo simulations (Zein et al., 2018), however, unlike the *in silico* predictions, the irradiance dependence *in vivo* is nonlinear.

During tPBM, 150-mW/cm^2 consistently produced larger beta and gamma power increases relative to 100 mW/cm^2, whereas no significant difference was found between 200 mW/cm^2 and 100 mW/cm^2. Post-tPBM, 150-mW/cm^2 produced larger alpha responses in almost all regions and continued to produce stronger beta responses, particularly in the temporal region, while again no significant variation was observed using 200 mW/cm^2. These findings demonstrate a clear biphasic response profile where an intermediate irradiance elicits the most robust neuromodulation, consistent with predictions based on cell-culture studies (Hamblin, 2016; Huang et al., 2011).

Within cells, optimal irradiance ensures efficient photoexcitation of CCO, leading to enhanced electron transport, ATP production, and redox signaling, all of which support fast, energy-intensive oscillations such as beta/gamma rhythms. Insufficient irradiance may fall below the threshold required to augment ATP synthesis, whereas excessive levels can trigger transient oxidative stress or dampen mitochondrial responsiveness (Huang et al., 2011; Pope & Denton, 2023). Thus, the larger high-frequency power increases at 150 mW/cm^2 likely reflect a “sweet spot” where neurons received sufficient metabolic support without reaching photochemical saturation.

Collectively, the core parameter dependencies identified in our data emphasize that no single parameter is enough to determine tPBM efficacy. Parameters should be selected based on target chromophores and frequency bands to convert photonic energy into desired neurophysiological changes. That said, for improving cognitive function and to directly influence beta/gamma activity, our findings reflect that 150 mW/cm^2 may be a strong, near optimal irradiance level to use, however, parameter interactions should always be considered.

4.5 Biological moderators of the EEG response

Individual biological characteristics strongly influence how tPBM energy is transmitted to the cortex. Our analyses revealed that skin tone and sex were significant moderators of EEG responses

4.5.1 Skin tone and melanin-dependent dose delivery

Epidermal melanin concentration is a key determinant of how NIR light travels through biological tissue. Melanin acts as an absorber that attenuates incident photons before they reach deeper layers, thereby reducing the effective energy available for absorption by mitochondria or other tissue structures. Individual differences in epidermal melanin, as a prominent chromophore, directly affects light penetration, scattering, and absorption within neural tissues (Cassano et al., 2019; Li et al., 2017; Palamoni et al., 2022; Van Lankveld et al., 2025). In our data, lighter skin tone was linked to significantly larger online alpha response in the prefrontal region and gamma responses across central, parietal, and occipital regions. In the offline period, skin tone effects were modulated by sex; in the prefrontal region, lighter skin was associated with larger alpha responses in females whereas darker skin was associated with larger alpha responses in males.

Recent simulations from our group further quantified this effect. Using Monte Carlo stimulations, Van Lankveld et al. demonstrated that lighter skin allows for higher energy accumulation in the cortex; up to 16% of incident 810 nm light in the rostral dorsal PFC, whereas the darkest simulated skin tone achieved only 6% (Van Lankveld et al., 2025). This means that to reach the same cortical energy deposition observed in lighter skin, more than twice the surface irradiance would be required for darker skin tones. This enhanced photon delivery in lighter skin is could be attributed to

lower levels of eumelanin, which absorbs strongly in the NIR range, and aligns with studies linking reduced eumelanin levels to lower light absorption in the epidermis (Zhang et al., 2023).

As a result, melanin-dependent absorption likely accounts for a substantial portion of the inter-subject variability in tPBM-induced EEG power modulation. These findings underscore the need for individualized dosimetry or adaptive irradiance scaling in future tPBM protocols to achieve comparable neuromodulatory efficacy across diverse populations.

4.5.2 Sex differences and interactions with parameters

Sex-related variability in cortical structure and oscillatory dynamics are well-documented and likely contribute to individual differences in tPBM responsiveness. Our data revealed significant sex-specific EEG effects post-tPBM that were modulated by wavelength and frequency, with other factors at reference values (100 mW/cm^2, lighter skin). Using 808 nm-10 Hz, females exhibited larger delta power increases in the central region and stronger beta power responses in the occipital relative to males. Conversely, under 1064 nm-10 Hz, males showed greater alpha power increases, especially in the prefrontal region, and beta power increases, especially in the occipital region. Finally, using 808 nm-40 Hz, males displayed larger delta power increases in the central region.

The parameter-dependent nature of these effects suggests that anatomical and neuroenergetic sex differences, potentially mediated by estrogen-sensitive mitochondrial dynamics, modulate how photobiological energy is coupled to neural circuit dynamics. Females typically have thicker cortices than males, particularly in the left hemisphere, while males show relatively greater cortical thickness in the right hemisphere (Sowell et al., 2008; Zaidi, 2010). These differences have been shown to correlate with distinct baseline oscillatory profiles with females generally displaying higher beta/gamma power (Brenner et al., 1995). A magnetoencephalography (MEG) study further reported that females have higher beta power than males (Zappasodi et al., 2006), and an EEG study found that prefrontal absolute power is higher in females than males (Morgan et al., 2005). Furthermore, males tend to show stronger low-frequency power in the left caudal region, while females show stronger high-frequency power in the right caudal region (Sowell et al., 2008; Zaidi, 2010). Cortical thickness is positively correlated with gamma power (van Pelt et al., 2018), suggesting that these structural differences may underlie sex-specific patterns of fast oscillatory activity.

Collectively, these findings reinforce that sex is not merely a covariate, but a biologically relevant moderator of cortical PBM.

4.6 Limitations and future work

While our work revealed significant determinants of band-specific tPBM-induced EEG responses, several limitations constrain the generalizability and clinical translation of our findings. First, this study is limited to examining the effect of dose parameters, skin tone and sex in healthy young adults. Given our findings of pronounced skin tone and sex dependencies, future studies could examine how changes in melanin distribution and hormonal fluctuations across ages interact with the parameter effects we identified. tPBM was also applied exclusively to the rPFC, restricting insights into parameter effects at other critical sites such as DMN nodes or the motor cortex due to their relevance in neurodegenerative diseases. The regional specificity we observed further suggests that optimal parameters may be site-dependent. Future work could compare parameter responses across multiple brain regions to determine whether our prefrontal findings generalize or require region-specific optimization, especially in more vulnerable populations.

Additionally, our irradiance range, while physiologically relevant, may not capture the full therapeutic window. Testing was limited to 100-200 mW/cm^2 to avoid thermal sensations, potentially missing higher intensities that could reveal biphasic dose-response patterns predicted by PBM theory (Huang et al., 2011). The temporal resolution of our analysis, while revealing distinct online versus offline patterns, cannot capture the full time-course of tPBM effects. Our short during and post-tPBM analysis windows may miss later longer-lasting changes that may appear minutes to potentially even hours post-treatment which could inform optimal treatment scheduling. Variations in the distance between the laser and the cortex were also not accounted for as this required precisely measuring each

tissue layer's optical properties of light scattering and absorption which were not feasible due to insufficient data.

Integrating EEG with hemodynamic imaging (e.g., fMRI) would also help clarify how tPBM influences vascular pathways. Such multimodal approaches could enable simultaneous measurement of cerebral blood flow, cerebral metabolic rate of oxygen consumption ($CMRO_2$), and neural oscillatory activity, providing crucial insights into whether the observed EEG changes reflect direct mitochondrial stimulation, improved cerebrovascular function, or both. Finally, exploring delivery routes that minimize melanin interference, like intranasal application, could broaden accessibility and efficacy, a treatment approach we plan to investigate in the future.

5 CONCLUSION

This is the first study to show that forehead tPBM in healthy young adults results in prolonged modulation of high-frequency EEG power, lasting four minutes after stimulation ends, and that this neural response depends on interactions between wavelength, frequency, irradiance, skin tone, and sex, stressing the need for personalized protocols. We demonstrate that 808 nm-10 Hz and 1064 nm-40 Hz laser combinations can be strategically utilized for stronger and longer-lasting high-frequency oscillatory enhancement compared to 808 nm-40 Hz and 1064 nm-10 Hz. Furthermore, consistently larger responses in lighter skin tones and sex dependencies demonstrate that demographic factors are not merely confounding variables but critical determinants of treatment efficacy. These findings necessitate the development of individualized dosing protocols that account for optical and physiological differences to ensure equitable therapeutic outcomes across diverse populations. By establishing EEG as a real-time biomarker of tPBM's neuromodulatory effects, our results provide a roadmap for advancing tPBM from a one-size-fits-all approach toward more precise protocols.

6 ACKNOWLEDGMENTS

This work was funded by the Ontario Centre for Innovation, the Natural Sciences and Engineering Research Council of Canada, Ydessa Hendeles Graduate Scholarship, and Vielight Inc.

7 REFERENCES

Allen, N. J. (2014). Astrocyte regulation of synaptic behavior. *Annual Review of Cell and Developmental Biology*, *30*(1), 439–463. https://doi.org/10.1146/annurev-cellbio-100913-013053

Attwell, D., & Laughlin, S. B. (2001). An energy budget for signaling in the grey matter of the brain. *Journal of Cerebral Blood Flow and Metabolism: Official Journal of the International Society of Cerebral Blood Flow and Metabolism*, *21*(10), 1133–1145. https://doi.org/10.1097/00004647-200110000-00001

Barrett, D. W., & Gonzalez-Lima, F. (2013). Transcranial infrared laser stimulation produces beneficial cognitive and emotional effects in humans. *Neuroscience*, *230*, 13–23. https://doi.org/10.1016/j.neuroscience.2012.11.016

Bashir, S., Al-Hussain, F., Hamza, A., Shareefi, G. F., Abualait, T., & Yoo, W.-K. (2020). Role of single low pulse intensity of transcranial magnetic stimulation over the frontal cortex for cognitive function. *Frontiers in Human Neuroscience*, *14*, 205. https://doi.org/10.3389/fnhum.2020.00205

Benjamini, Y., & Hochberg, Y. (1995). Controlling the false discovery rate: A practical and powerful approach to multiple testing. *Journal of the Royal Statistical Society. Series B, Statistical Methodology*, *57*(1), 289–300. https://doi.org/10.1111/j.2517-6161.1995.tb02031.x

Berger, H. (1929). Über das Elektrenkephalogramm des Menschen. *Archiv für Psychiatrie und Nervenkrankheiten*, *87*(1), 527–570. https://doi.org/10.1007/bf01797193

Blanco-Duque, C., Chan, D., Kahn, M. C., Murdock, M. H., & Tsai, L.-H. (2024). Audiovisual gamma stimulation for the treatment of neurodegeneration. *Journal of Internal Medicine*, *295*(2), 146–170. https://doi.org/10.1111/joim.13755

Blivet, G., Touchon, B., Cavadore, H., Guillemin, S., Pain, F., Weiner, M., … Touchon, J. (2025). Brain photobiomodulation: a potential treatment in Alzheimer's and Parkinson's diseases. *The Journal of Prevention of Alzheimer's Disease*, *12*(7), 100185. https://doi.org/10.1016/j.tjpad.2025.100185

Brenner, R. P., Ulrich, R. F., & Reynolds, C. F., 3rd. (1995). EEG spectral findings in healthy, elderly men and women--sex differences. *Electroencephalography and Clinical Neurophysiology*, *94*(1), 1–5. https://doi.org/10.1016/0013-4694(94)00234-c

Buzsáki, G., & Wang, X.-J. (2012). Mechanisms of gamma oscillations. *Annual Review of Neuroscience*, *35*(1), 203–225. https://doi.org/10.1146/annurev-neuro-062111-150444

Cardin, J. A., Carlén, M., Meletis, K., Knoblich, U., Zhang, F., Deisseroth, K., … Moore, C. I. (2009). Driving fast-spiking cells induces gamma rhythm and controls sensory responses. *Nature*, *459*(7247), 663–667. https://doi.org/10.1038/nature08002

Cassano, P., Tran, A. P., Katnani, H., Bleier, B. S., Hamblin, M. R., Yuan, Y., & Fang, Q. (2019). Selective photobiomodulation for emotion regulation: model-based dosimetry study. *Neurophotonics*, *6*(1), 015004. https://doi.org/10.1117/1.NPh.6.1.015004

Chan, A. S., Lee, T. L., Yeung, M. K., & Hamblin, M. R. (2019). Photobiomodulation improves the frontal cognitive function of older adults. *International Journal of Geriatric Psychiatry*, *34*(2), 369–377. https://doi.org/10.1002/gps.5039

Chen, X., Lv, Z., Xie, G., Zhao, C., Zhou, Y., Fu, F., … Chen, Y. (2025). Unleashing the potential: 40 Hz multisensory stimulation therapy for cognitive impairment. *Journal of Central Nervous System Disease*, *17*, 11795735251328029. https://doi.org/10.1177/11795735251328029

de Freitas, L. F., & Hamblin, M. R. (2016). Proposed mechanisms of photobiomodulation or low-level light therapy. *IEEE Journal of Selected Topics in Quantum Electronics: A Publication of the IEEE Lasers and Electro-Optics Society*, *22*(3), 348–364. https://doi.org/10.1109/JSTQE.2016.2561201

Drew, P. J. (2022). Neurovascular coupling: motive unknown. *Trends in Neurosciences*, *45*(11), 809–819. https://doi.org/10.1016/j.tins.2022.08.004

Engel, A. K., & Fries, P. (2010). Beta-band oscillations--signalling the status quo? *Current Opinion in Neurobiology*, *20*(2), 156–165. https://doi.org/10.1016/j.conb.2010.02.015

Fano, S., Behrens, C. J., & Heinemann, U. (2007). Hypoxia suppresses kainate-induced gamma-oscillations in rat hippocampal slices. *Neuroreport*, *18*(17), 1827–1831. https://doi.org/10.1097/WNR.0b013e3282f13e4f

Fernandez-Ruiz, A., Sirota, A., Lopes-Dos-Santos, V., & Dupret, D. (2023). Over and above frequency: Gamma oscillations as units of neural circuit operations. *Neuron*, *111*(7), 936–953. https://doi.org/10.1016/j.neuron.2023.02.026

Gal, S., Coldham, Y., Tik, N., Bernstein-Eliav, M., & Tavor, I. (2022). Act natural: Functional connectivity from naturalistic stimuli fMRI outperforms resting-state in predicting brain activity. *NeuroImage*, *258*(119359), 119359. https://doi.org/10.1016/j.neuroimage.2022.119359

Gillespie, J. B., Maclean, M., Given, M. J., Wilson, M. P., Judd, Timoshkin, I. V., & MacGregor, S. J. (2017). Efficacy of Pulsed 405-nm Light-Emitting Diodes for Antimicrobial Photodynamic Inactivation: Effects of Intensity, Frequency, and Duty Cycle. *Photomedicine and Laser Surgery*, *35*(3). https://doi.org/10.1089/pho.2016.4179

Gola, M., Kamiński, J., Brzezicka, A., & Wróbel, A. (2012). B band oscillations as a correlate of alertness--changes in aging. *International Journal of Psychophysiology: Official Journal of the International Organization of Psychophysiology*, *85*(1), 62–67. https://doi.org/10.1016/j.ijpsycho.2011.09.001

Gonzalez-Lima, F., & Barrett, D. W. (2014). Augmentation of cognitive brain functions with transcranial lasers. *Frontiers in Systems Neuroscience*, *8*. https://doi.org/10.3389/fnsys.2014.00036

Grass, F., Klima, H., & Kasper, S. (2004). Biophotons, microtubules and CNS, is our brain a "holographic computer"? *Medical Hypotheses*, *62*(2), 169–172. https://doi.org/10.1016/S0306-9877(03)00308-6

Haber, S. N., & Robbins, T. (2022). The prefrontal cortex. *Neuropsychopharmacology: Official Publication of the American College of Neuropsychopharmacology*, *47*(1), 1–2. https://doi.org/10.1038/s41386-021-01184-2

Hamblin, M. R. (2016). Shining light on the head: Photobiomodulation for brain disorders. *BBA Clinical*, *6*, 113–124. https://doi.org/10.1016/j.bbacli.2016.09.002

Hamblin, M. R. (2018). Mechanisms and mitochondrial redox signaling in photobiomodulation.

Photochemistry and Photobiology, *94*(2), 199–212. https://doi.org/10.1111/php.12864
Harmony, T. (2013). The functional significance of delta oscillations in cognitive processing. *Frontiers in Integrative Neuroscience*, *7*, 83. https://doi.org/10.3389/fnint.2013.00083
Harris, J. J., & Attwell, D. (2012). The energetics of CNS white matter. *The Journal of Neuroscience: The Official Journal of the Society for Neuroscience*, *32*(1), 356–371. https://doi.org/10.1523/JNEUROSCI.3430-11.2012
Hashmi, J. T., Huang, Y.-Y., Sharma, S. K., Kurup, D. B., De Taboada, L., Carroll, J. D., & Hamblin, M. R. (2010). Effect of pulsing in low-level light therapy. *Lasers in Surgery and Medicine*, *42*(6), 450–466. https://doi.org/10.1002/lsm.20950
Henderson, T. A., & Morries, L. D. (2015). Near-infrared photonic energy penetration: can infrared phototherapy effectively reach the human brain? *Neuropsychiatric Disease and Treatment*, *11*, 2191–2208. https://doi.org/10.2147/NDT.S78182
Hennessy, M., & Hamblin, M. R. (2017). Photobiomodulation and the brain: a new paradigm. *Journal of Optics (2010)*, *19*(1), 013003. https://doi.org/10.1088/2040-8986/19/1/013003
Herweg, N. A., Apitz, T., Leicht, G., Mulert, C., Fuentemilla, L., & Bunzeck, N. (2016). Theta-alpha oscillations bind the hippocampus, prefrontal cortex, and striatum during recollection: Evidence from simultaneous EEG-fMRI. *The Journal of Neuroscience: The Official Journal of the Society for Neuroscience*, *36*(12), 3579–3587. https://doi.org/10.1523/JNEUROSCI.3629-15.2016
Hosford, P. S., & Gourine, A. V. (2019). What is the key mediator of the neurovascular coupling response? *Neuroscience and Biobehavioral Reviews*, *96*, 174–181. https://doi.org/10.1016/j.neubiorev.2018.11.011
Howarth, C., Gleeson, P., & Attwell, D. (2012). Updated energy budgets for neural computation in the neocortex and cerebellum. *Journal of Cerebral Blood Flow and Metabolism: Official Journal of the International Society of Cerebral Blood Flow and Metabolism*, *32*(7), 1222–1232. https://doi.org/10.1038/jcbfm.2012.35
Huang, Y.-Y., Sharma, S. K., Carroll, J., & Hamblin, M. R. (2011). Biphasic dose response in low level light therapy - an update. *Dose-Response: A Publication of International Hormesis Society*, *9*(4), 602–618. https://doi.org/10.2203/dose-response.11-009.Hamblin
Iaccarino, H. F., Singer, A. C., Martorell, A. J., Rudenko, A., Gao, F., Gillingham, T. Z., … Tsai, L.-H. (2016). Gamma frequency entrainment attenuates amyloid load and modifies microglia. *Nature*, *540*(7632), 230–235. https://doi.org/10.1038/nature20587
Iaccarino, H. F., Singer, A. C., Martorell, A. J., Rudenko, A., Gao, F., Gillingham, T. Z., … Tsai, L.-H. (2024). Author Correction: Gamma frequency entrainment attenuates amyloid load and modifies microglia. *Nature*, *636*(8042), E2. https://doi.org/10.1038/s41586-024-08343-7
Illes, P., Burnstock, G., & Tang, Y. (2019). Astroglia-derived ATP modulates CNS neuronal circuits. *Trends in Neurosciences*, *42*(12), 885–898. https://doi.org/10.1016/j.tins.2019.09.006
Kann, O. (2011). The energy demand of fast neuronal network oscillations: insights from brain slice preparations. *Frontiers in Pharmacology*, *2*, 90. https://doi.org/10.3389/fphar.2011.00090
Kann, O., Huchzermeyer, C., Kovács, R., Wirtz, S., & Schuelke, M. (2011). Gamma oscillations in the hippocampus require high complex I gene expression and strong functional performance of mitochondria. *Brain: A Journal of Neurology*, *134*(Pt 2), 345–358. https://doi.org/10.1093/brain/awq333
Kann, O., Papageorgiou, I. E., & Draguhn, A. (2014). Highly energized inhibitory interneurons are a central element for information processing in cortical networks. *Journal of Cerebral Blood Flow and Metabolism: Official Journal of the International Society of Cerebral Blood Flow and Metabolism*, *34*(8), 1270–1282. https://doi.org/10.1038/jcbfm.2014.104
Karakaş, S. (2020). A review of theta oscillation and its functional correlates. *International Journal of Psychophysiology: Official Journal of the International Organization of Psychophysiology*, *157*, 82–99. https://doi.org/10.1016/j.ijpsycho.2020.04.008
Keshri, G. K., Gupta, A., Yadav, A., Sharma, S. K., & Singh, S. B. (2016). Photobiomodulation with pulsed and continuous wave near-infrared laser (810 nm, Al-Ga-as) augments dermal wound healing in immunosuppressed rats. *PloS One*, *11*(11), e0166705. https://doi.org/10.1371/journal.pone.0166705
Kim, H. B., Baik, K. Y., Choung, P.-H., & Chung, J. H. (2017). Pulse frequency dependency of photobiomodulation on the bioenergetic functions of human dental pulp stem cells. *Scientific*

Reports, *7*(1), 15927. https://doi.org/10.1038/s41598-017-15754-2
Klimesch, W. (1999). EEG alpha and theta oscillations reflect cognitive and memory performance: a review and analysis. *Brain Research. Brain Research Reviews*, *29*(2-3), 169–195. https://doi.org/10.1016/s0165-0173(98)00056-3
Klimesch, W., Doppelmayr, M., Stadler, W., Pöllhuber, D., Sauseng, P., & Röhm, D. (2001). Episodic retrieval is reflected by a process specific increase in human electroencephalographic theta activity. *Neuroscience Letters*, *302*(1), 49–52. https://doi.org/10.1016/s0304-3940(01)01656-1
Léger, D., Debellemaniere, E., Rabat, A., Bayon, V., Benchenane, K., & Chennaoui, M. (2018). Slow-wave sleep: From the cell to the clinic. *Sleep Medicine Reviews*, *41*, 113–132. https://doi.org/10.1016/j.smrv.2018.01.008
Liebert, A., Capon, W., Pang, V., Vila, D., Bicknell, B., McLachlan, C., & Kiat, H. (2023). Photophysical mechanisms of photobiomodulation therapy as precision medicine. *Biomedicines*, *11*(2), 237. https://doi.org/10.3390/biomedicines11020237
Liebert, A. D., Bicknell, B. T., & Adams, R. D. (2014). Protein conformational modulation by photons: a mechanism for laser treatment effects. *Medical Hypotheses*, *82*(3), 275–281. https://doi.org/10.1016/j.mehy.2013.12.009
Li, T., Xue, C., Wang, P., Li, Y., & Wu, L. (2017). Photon penetration depth in human brain for light stimulation and treatment: A realistic Monte Carlo simulation study. *Journal of Innovative Optical Health Sciences*, *10*(05), 1743002. https://doi.org/10.1142/S1793545817430027
Liu, C., Han, T., Xu, Z., Liu, J., Zhang, M., Du, J., ... Wang, Y. (2022). Modulating gamma oscillations promotes brain connectivity to improve cognitive impairment. *Cerebral Cortex (New York, N.Y.: 1991)*, *32*(12), 2644–2656. https://doi.org/10.1093/cercor/bhab371
Lyu, S., He, Y., Tao, X., Yao, Y., Huang, X., Ma, Y., ... Wang, Y. (2022). Subcutaneous power supply by NIR-II light. *Nature Communications*, *13*(1), 6596. https://doi.org/10.1038/s41467-022-34047-5
Manyukhina, V. O., Rostovtseva, E. N., Prokofyev, A. O., Obukhova, T. S., Schneiderman, J. F., Stroganova, T. A., & Orekhova, E. V. (2021). Visual gamma oscillations predict sensory sensitivity in females as they do in males. *Scientific Reports*, *11*(1), 12013. https://doi.org/10.1038/s41598-021-91381-2
Miller, E. K., Lundqvist, M., & Bastos, A. M. (2018). Working memory 2.0. *Neuron*, *100*(2), 463–475. https://doi.org/10.1016/j.neuron.2018.09.023
Moore, C. I., & Cao, R. (2008). The hemo-neural hypothesis: on the role of blood flow in information processing. *Journal of Neurophysiology*, *99*(5), 2035–2047. https://doi.org/10.1152/jn.01366.2006
Morgan, M. L., Witte, E. A., Cook, I. A., Leuchter, A. F., Abrams, M., & Siegman, B. (2005). Influence of age, gender, health status, and depression on quantitative EEG. *Neuropsychobiology*, *52*(2), 71–76. https://doi.org/10.1159/000086608
Mothersill, C., Le, M., Rusin, A., & Seymour, C. (2019). Biophotons in radiobiology: Inhibitors, communicators and reactors. *Radiation Protection Dosimetry*, *183*(1-2), 136–141. https://doi.org/10.1093/rpd/ncy271
Nahas, Z., Teneback, C. C., Kozel, A., Speer, A. M., DeBrux, C., Molloy, M., ... George, M. S. (2001). Brain effects of TMS delivered over prefrontal cortex in depressed adults: role of stimulation frequency and coil-cortex distance. *The Journal of Neuropsychiatry and Clinical Neurosciences*, *13*(4), 459–470. https://doi.org/10.1176/jnp.13.4.459
Niessing, J., Ebisch, B., Schmidt, K. E., Niessing, M., Singer, W., & Galuske, R. A. W. (2005). Hemodynamic signals correlate tightly with synchronized gamma oscillations. *Science (New York, N.Y.)*, *309*(5736), 948–951. https://doi.org/10.1126/science.1110948
Nortley, R., & Attwell, D. (2017). Control of brain energy supply by astrocytes. *Current Opinion in Neurobiology*, *47*, 80–85. https://doi.org/10.1016/j.conb.2017.09.012
Nunez, P. L., & Srinivasan, R. (2005). *Electric fields of the brain* (2nd ed.). New York, NY: Oxford University Press. https://doi.org/10.1093/acprof:oso/9780195050387.001.0001
Oron, U., Ilic, S., De Taboada, L., & Streeter, J. (2007). Ga-As (808 nm) laser irradiation enhances ATP production in human neuronal cells in culture. *Photomedicine and Laser Surgery*, *25*(3), 180–182. https://doi.org/10.1089/pho.2007.2064
Palacios-García, I., Silva, J., Villena-González, M., Campos-Arteaga, G., Artigas-Vergara, C., Luarte, N., ... Bosman, C. A. (2021). Increase in beta power reflects attentional top-down modulation after psychosocial stress induction. *Frontiers in Human Neuroscience*, *15*, 630813.

https://doi.org/10.3389/fnhum.2021.630813
Palamoni, O. P., de Magalhães, A. C., Moriyama, L. T., de Sousa, M. V. P., & Fortunato, T. C. (2022). Monte Carlo simulations to study light propagation through the skin of different phototypes. *Tissue Optics and Photonics II*, *12147*, 28–34. SPIE. https://doi.org/10.1117/12.2621670
Park, J. M., & Tsai, L.-H. (2025). Innovations in noninvasive sensory stimulation treatments to combat Alzheimer's disease. *PLoS Biology*, *23*(2), e3003046. https://doi.org/10.1371/journal.pbio.3003046
Pietersen, A. N., Lancaster, D. M., Patel, N., Hamilton, J. B., & Vreugdenhil, M. (2009). Modulation of gamma oscillations by endogenous adenosine through A1 and A2A receptors in the mouse hippocampus. *Neuropharmacology*, *56*(2), 481–492. https://doi.org/10.1016/j.neuropharm.2008.10.001
Pope, N. J., & Denton, M. L. (2023). Differential effects of 808-nm light on electron transport chain enzymes in isolated mitochondria: Implications for photobiomodulation initiation. *Mitochondrion*, *68*, 15–24. https://doi.org/10.1016/j.mito.2022.11.002
Pruitt, T., Davenport, E. M., Proskovec, A. L., Maldjian, J. A., & Liu, H. (2024). Simultaneous MEG and EEG source imaging of electrophysiological activity in response to acute transcranial photobiomodulation. *Frontiers in Neuroscience*, *18*, 1368172. https://doi.org/10.3389/fnins.2024.1368172
Reddy, O. C., & van der Werf, Y. D. (2020). The sleeping brain: Harnessing the power of the glymphatic system through lifestyle choices. *Brain Sciences*, *10*(11), 868. https://doi.org/10.3390/brainsci10110868
Sachdev, R. N. S., Gaspard, N., Gerrard, J. L., Hirsch, L. J., Spencer, D. D., & Zaveri, H. P. (2015). Delta rhythm in wakefulness: evidence from intracranial recordings in human beings. *Journal of Neurophysiology*, *114*(2), 1248–1254. https://doi.org/10.1152/jn.00249.2015
Salari, V., Valian, H., Bassereh, H., Bókkon, I., & Barkhordari, A. (2015). Ultraweak photon emission in the brain. *Journal of Integrative Neuroscience*, *14*(3), 419–429. https://doi.org/10.1142/S0219635215300012
Salehpour, F., Mahmoudi, J., Kamari, F., Sadigh-Eteghad, S., Rasta, S. H., & Hamblin, M. R. (2018). Brain photobiomodulation therapy: A narrative review. *Molecular Neurobiology*, *55*(8), 6601–6636. https://doi.org/10.1007/s12035-017-0852-4
Sandell, J. L., & Zhu, T. C. (2011). A review of in-vivo optical properties of human tissues and its impact on PDT. *Journal of Biophotonics*, *4*(11-12), 773–787. https://doi.org/10.1002/jbio.201100062
Saucedo, C. L., Courtois, E. C., Wade, Z. S., Kelley, M. N., Kheradbin, N., Barrett, D. W., & Gonzalez-Lima, F. (2021). Transcranial laser stimulation: Mitochondrial and cerebrovascular effects in younger and older healthy adults. *Brain Stimulation*, *14*(2), 440–449. https://doi.org/10.1016/j.brs.2021.02.011
Schmidt, R., Herrojo Ruiz, M., Kilavik, B. E., Lundqvist, M., Starr, P. A., & Aron, A. R. (2019). Beta oscillations in working memory, executive control of movement and thought, and sensorimotor function. *The Journal of Neuroscience: The Official Journal of the Society for Neuroscience*, *39*(42), 8231–8238. https://doi.org/10.1523/JNEUROSCI.1163-19.2019
Shahdadian, S., Wang, X., Wanniarachchi, H., Chaudhari, A., Truong, N. C. D., & Liu, H. (2022). Neuromodulation of brain power topography and network topology by prefrontal transcranial photobiomodulation. *Journal of Neural Engineering*, *19*(6), 066013. https://doi.org/10.1088/1741-2552/ac9ede
Shapiro, M. G., Homma, K., Villarreal, S., Richter, C.-P., & Bezanilla, F. (2017). Correction: Corrigendum: Infrared light excites cells by changing their electrical capacitance. *Nature Communications*, *8*(1), 16148. https://doi.org/10.1038/ncomms16148
Sharma, S. K., Sardana, S., & Hamblin, M. R. (2023). Role of opsins and light or heat activated transient receptor potential ion channels in the mechanisms of photobiomodulation and infrared therapy. *Journal of Photochemistry and Photobiology*, *13*(100160), 100160. https://doi.org/10.1016/j.jpap.2023.100160
Shen, Q., Guo, H., & Yan, Y. (2024). Photobiomodulation for neurodegenerative diseases: A scoping review. *International Journal of Molecular Sciences*, *25*(3). https://doi.org/10.3390/ijms25031625
Sowell, E. R., Mattson, S. N., Kan, E., Thompson, P. M., Riley, E. P., & Toga, A. W. (2008). Abnormal cortical thickness and brain-behavior correlation patterns in individuals with heavy prenatal alcohol exposure. *Cerebral Cortex (New York, N.Y.: 1991)*, *18*(1), 136–144.

https://doi.org/10.1093/cercor/bhm039
Spera, V., Sitnikova, T., Ward, M. J., Farzam, P., Hughes, J., Gazecki, S., … Cassano, P. (2021). Pilot study on dose-dependent effects of transcranial photobiomodulation on brain electrical oscillations: A potential therapeutic target in Alzheimer's disease. *Journal of Alzheimer's Disease: JAD*, *83*(4), 1481–1498. https://doi.org/10.3233/JAD-210058
Stroganova, T. A., Butorina, A. V., Sysoeva, O. V., Prokofyev, A. O., Nikolaeva, A. Y., Tsetlin, M. M., & Orekhova, E. V. (2015). Altered modulation of gamma oscillation frequency by speed of visual motion in children with autism spectrum disorders. *Journal of Neurodevelopmental Disorders*, *7*(1), 21. https://doi.org/10.1186/s11689-015-9121-x
Tang, L., Jiang, H., Sun, M., & Liu, M. (2023). Pulsed transcranial photobiomodulation generates distinct beneficial neurocognitive effects compared with continuous wave transcranial light. *Lasers in Medical Science*, *38*(1), 203. https://doi.org/10.1007/s10103-023-03865-4
Tang, L., Qin, H., Lin, S., & Liu, M. (2023). Effects of pulsed red and near-infrared light on neuroblastoma cells—pilot study on frequency and duty cycle. *Photonics*, *10*(3), 315. https://doi.org/10.3390/photonics10030315
Tang, R., & Dai, J. (2014). Biophoton signal transmission and processing in the brain. *Journal of Photochemistry and Photobiology. B, Biology*, *139*, 71–75. https://doi.org/10.1016/j.jphotobiol.2013.12.008
Theriault, J. E., Shaffer, C., Dienel, G. A., Sander, C. Y., Hooker, J. M., Dickerson, B. C., … Quigley, K. S. (2023). A functional account of stimulation-based aerobic glycolysis and its role in interpreting BOLD signal intensity increases in neuroimaging experiments. *Neuroscience and Biobehavioral Reviews*, *153*(105373), 105373. https://doi.org/10.1016/j.neubiorev.2023.105373
Thut, G., Miniussi, C., & Gross, J. (2012). The functional importance of rhythmic activity in the brain. *Current Biology: CB*, *22*(16), R658–R663. https://doi.org/10.1016/j.cub.2012.06.061
Traub, R. (2000). Fast Oscillations in Cortical Circuits. *International Journal of Neural Systems*, *10*(2), 155–157. https://doi.org/10.1016/s0129-0657(00)00013-2
van Kerkoerle, T., Self, M. W., Dagnino, B., Gariel-Mathis, M.-A., Poort, J., van der Togt, C., & Roelfsema, P. R. (2014). Alpha and gamma oscillations characterize feedback and feedforward processing in monkey visual cortex. *Proceedings of the National Academy of Sciences of the United States of America*, *111*(40), 14332–14341. https://doi.org/10.1073/pnas.1402773111
Van Lankveld, H., Mai, A. Q., Lim, L., Hosseinkhah, N., Cassano, P., & Jean Chen, J. (2025). Simulation-based dosimetry of transcranial and intranasal photobiomodulation of the human brain: the roles of wavelength, power density, and skin tone. *Biomedical Optics Express*, *16*(8), 3295–3314. https://doi.org/10.1364/BOE.567345
van Pelt, S., Shumskaya, E., & Fries, P. (2018). Cortical volume and sex influence visual gamma. *NeuroImage*, *178*, 702–712. https://doi.org/10.1016/j.neuroimage.2018.06.005
Van Wijk, R., Van Wijk, E. P. A., Pang, J., Yang, M., Yan, Y., & Han, J. (2020). Integrating ultra-weak photon emission analysis in mitochondrial research. *Frontiers in Physiology*, *11*, 717. https://doi.org/10.3389/fphys.2020.00717
Vargas, E., Barrett, D. W., Saucedo, C. L., Huang, L.-D., Abraham, J. A., Tanaka, H., … Gonzalez-Lima, F. (2017). Beneficial neurocognitive effects of transcranial laser in older adults. *Lasers in Medical Science*, *32*(5), 1153–1162. https://doi.org/10.1007/s10103-017-2221-y
Wang, J. B., Hassan, U., Bruss, J. E., Oya, H., Uitermarkt, B. D., Trapp, N. T., … Boes, A. D. (2024). Effects of transcranial magnetic stimulation on the human brain recorded with intracranial electrocorticography. *Molecular Psychiatry*, *29*(5), 1228–1240. https://doi.org/10.1038/s41380-024-02405-y
Wang, X., Dmochowski, J. P., Zeng, L., Kallioniemi, E., Husain, M., Gonzalez-Lima, F., & Liu, H. (2019). Transcranial photobiomodulation with 1064-nm laser modulates brain electroencephalogram rhythms. *Neurophotonics*, *6*(2), 025013. https://doi.org/10.1117/1.NPh.6.2.025013
Wang, X., Tian, F., Reddy, D. D., Nalawade, S. S., Barrett, D. W., Gonzalez-Lima, F., & Liu, H. (2017). Up-regulation of cerebral cytochrome-c-oxidase and hemodynamics by transcranial infrared laser stimulation: A broadband near-infrared spectroscopy study. *Journal of Cerebral Blood Flow and Metabolism: Official Journal of the International Society of Cerebral Blood Flow and Metabolism*, *37*(12), 3789–3802. https://doi.org/10.1177/0271678X17691783
Wang, X., Tian, F., Soni, S. S., Gonzalez-Lima, F., & Liu, H. (2016). Interplay between up-regulation of

cytochrome-c-oxidase and hemoglobin oxygenation induced by near-infrared laser. *Scientific Reports*, *6*(1). https://doi.org/10.1038/srep30540

Wang, X., Wanniarachchi, H., Wu, A., Gonzalez-Lima, F., & Liu, H. (2021). Transcranial photobiomodulation and thermal stimulation induce distinct topographies of EEG alpha and beta power changes in healthy humans. *Scientific Reports*, *11*(1), 18917. https://doi.org/10.1038/s41598-021-97987-w

Wang, Y., Huang, Y.-Y., Wang, Y., Lyu, P., & Hamblin, M. R. (2016). Photobiomodulation (blue and green light) encourages osteoblastic-differentiation of human adipose-derived stem cells: role of intracellular calcium and light-gated ion channels. *Scientific Reports*, *6*(1). https://doi.org/10.1038/srep33719

Whittaker, R. G., Turnbull, D. M., Whittington, M. A., & Cunningham, M. O. (2011). Impaired mitochondrial function abolishes gamma oscillations in the hippocampus through an effect on fast-spiking interneurons. *Brain: A Journal of Neurology*, *134*(Pt 7), e180; author reply e181. https://doi.org/10.1093/brain/awr018

Wong-Riley, M. T. T., Liang, H. L., Eells, J. T., Chance, B., Henry, M. M., Buchmann, E., … Whelan, H. T. (2005). Photobiomodulation directly benefits primary neurons functionally inactivated by toxins: role of cytochrome c oxidase. *The Journal of Biological Chemistry*, *280*(6), 4761–4771. https://doi.org/10.1074/jbc.M409650200

Yan, B., Zhou, J., Yan, F., Gao, M., Tang, J., Huang, L., & Luo, Y. (2025). Unlocking the potential of photobiomodulation therapy for brain neurovascular coupling: The biological effects and medical applications. *Journal of Cerebral Blood Flow and Metabolism: Official Journal of the International Society of Cerebral Blood Flow and Metabolism*, *45*(5), 800–830. https://doi.org/10.1177/0271678X241311695

Yuan, Y., Cassano, P., Pias, M., & Fang, Q. (2020). Transcranial photobiomodulation with near-infrared light from childhood to elderliness: simulation of dosimetry. *Neurophotonics*, *7*(1), 015009. https://doi.org/10.1117/1.NPh.7.1.015009

Zaidi, Z. F. (2010). Gender differences in human brain: A review. *The Open Anatomy Journal*, *2*, 37–55. https://doi.org/10.2174/1877609401002010037

Zangari, A., Micheli, D., Galeazzi, R., Tozzi, A., Balzano, V., Bellavia, G., & Caristo, M. E. (2021). Photons detected in the active nerve by photographic technique. *Scientific Reports*, *11*(1), 3022. https://doi.org/10.1038/s41598-021-82622-5

Zappasodi, F., Pasqualetti, P., Tombini, M., Ercolani, M., Pizzella, V., Rossini, P. M., & Tecchio, F. (2006). Hand cortical representation at rest and during activation: gender and age effects in the two hemispheres. *Clinical Neurophysiology: Official Journal of the International Federation of Clinical Neurophysiology*, *117*(7), 1518–1528. https://doi.org/10.1016/j.clinph.2006.03.016

Zein, R., Selting, W., & Hamblin, M. R. (2018). Review of light parameters and photobiomodulation efficacy: dive into complexity. *Journal of Biomedical Optics*, *23*(12), 1–17. https://doi.org/10.1117/1.JBO.23.12.120901

Zhang, J., Treyer, V., Sun, J., Zhang, C., Gietl, A., Hock, C., … Alzheimer's Disease Neuroimaging Initiative. (2023). Automatic analysis of skull thickness, scalp-to-cortex distance and association with age and sex in cognitively normal elderly. *Brain Stimulation*, *16*(2), 653–656. https://doi.org/10.1016/j.brs.2023.03.011

Zomorrodi, R., Loheswaran, G., Pushparaj, A., & Lim, L. (2019). Pulsed Near Infrared Transcranial and Intranasal Photobiomodulation Significantly Modulates Neural Oscillations: a pilot exploratory study. *Scientific Reports*, *9*(1), 6309. https://doi.org/10.1038/s41598-019-42693-x